buildings

MDPI

*Article*

# An Investigation into the Distribution of Fluctuating Wind Pressure and Associated Probabilistic Characteristics of Low-Rise Buildings Impacted by the Gap between the Hillside and the Building

**Min Zhong [1,2,*], Chao Wang [2], Minghui Lin [3], Junyu Lu [3] and Xiangjun Wang [4]**

[1] School of Architecture and Engineering, Jiangsu Open University, Nanjing 210036, China
[2] College of Civil Engineering, Hunan University, Changsha 410082, China
[3] College of Civil Engineering, Hebei University of Architecture, Zhangjiakou 075000, China
[4] College of Electrical Energy and Power Engineering, Yangzhou University, Yangzhou 225127, China
* Correspondence: zhongmin@jsou.edu.cn; Tel.: +86-18013841138

**Abstract:** In China's mountainous coastal terrain, storms can badly damage low-rise buildings. At present, it is not clear how the relative position of buildings and mountains affects the surface of low-rise buildings. The study compared these results with the wind pressure distribution without the surrounding environment. The distribution of wind pressure in different hillside landforms is examined through a wind tunnel experiment, which is also compared with the distribution in an open environment. The study examined the fluctuating coefficient as the distance between the building and the hillside changed, specifically for wind blowing at a 0° angle. The investigation examined the power spectrum and wind pressure probability distribution while considering the proximity of the building to an adjacent hill. The findings indicated that as the distance between the slope and the mountain increases, the fluctuating wind pressure coefficient continues to increase, and the contour lines of the wind pressure distribution are relatively denser compared to where there is a mountain. The maximum value of the fluctuating wind pressure coefficient is 0.22, which appears at the windward roof. The roof's wind pressure coefficient fluctuated and gradually increased until it reached its peak, unaffected by the surroundings. The wind pressure on the leeward side exhibited Gaussian characteristics in its probability distribution.

**Keywords:** fluctuating wind pressure distribution; probabilistic properties; low-rise buildings; mountain form; the distance from the mountain

check for updates

**Citation:** Zhong, M.; Wang, C.; Lin, M.; Lu, J.; Wang, X. An Investigation into the Distribution of Fluctuating Wind Pressure and Associated Probabilistic Characteristics of Low-Rise Buildings Impacted by the Gap between the Hillside and the Building. *Buildings* **2024**, *14*, 1435. https://doi.org/10.3390/buildings14051435

Academic Editor: Francesco Ricciardelli

Received: 12 April 2024
Revised: 9 May 2024
Accepted: 11 May 2024
Published: 16 May 2024



## 1. Introduction

In the southeast coastal provinces of China, there is a significant quantity of low-lying structures, with the majority featuring double-sloped roofs and eaves. In the statistics of typhoon disaster losses, the collapse of low-rise buildings under mountains and the casualties caused by these account for a considerable proportion. As is shown in Figure 1, the low-rise buildings under the mountain terrain were significantly damaged affected by the typhoon. Hence, examining the wind pressure distribution of low-rise buildings and the impact of various mountain placements on wind loads is imperative. This will offer essential backing for the design of wind-resistant structures and the prevention of disasters in low-rise buildings.

**Figure 1.** A low-rise house collapsed in Rucheng County, Chenzhou City, Hunan province.

Under the terrain of mountain slopes, low buildings are influenced by the mountain and surrounding buildings, and the distribution of wind pressure is relatively complex. The wind load's interference effect between low-rise buildings is primarily influenced by factors such as wind direction, the ratio of spacing between adjacent buildings, the density and arrangement of building groups, as well as the height of surrounding buildings. Various researchers, both domestic and international, have conducted studies on the impact of wind load interference among low-rise structures. For instance, Fan Youchuan [1] and T. Van Hooff [2] examined the wind-induced interference effect on a single factory building as well as two consecutive factory buildings. They conducted wind tunnel tests to analyze the alterations in wind direction and building spacing. Akon and Kop [3] examined the wind pressure and re-attachment distance on a level rooftop while varying the incoming airflow's turbulence intensities. Their findings revealed that increasing the turbulence intensity of the incoming airflow reduces the re-attachment distance and increases the wind pressure. Holmes [4] examined the impact of wind-induced interference among multi-row structures and found that the alteration in spacing between preceding buildings and target structures had a more significant effect on the interference than the influence of preceding rows of buildings.

The impact of altering the density of the building area surrounding a structure of similar size on the flat roof's wind pressure coefficient was examined using a rigid model. It was determined that as the density of surrounding buildings increased, the maximum negative pressure on different areas of the target building's roof decreased and eventually became more consistent [5]. The roof's minimum wind pressure decreases on a single building when the area densities of the surrounding buildings increase. Chang et al. [6] and Yong et al. [7] showed that the distance between buildings and the height ratio between buildings will have a great influence on the "occlusion effect" of disturbed buildings. Wind tunnel experiments were conducted by Huai-Yu Zhong [8] to examine the impact of different sheltering conditions.

YONG C.K. [9] employed a wind tunnel testing technique to evaluate the wind load on a flat roof building model that was encircled by buildings of identical dimensions. The findings indicated that the disruptive element of the least favorable adverse wind pressure of the disrupted structure exceeds 1.0 when the nearby buildings have a low relative height. When the surrounding building's height is below 1.0, the interference factor declines as the surrounding building's height rises. However, when the surrounding building's height surpasses 1.0, the impact of height on the interference factor is not significant. The impact of various roof forms on the airflow around low-rise buildings was examined by Zhixiang Liu [10] and Tominaga et al. [11]. Researchers [12,13] conducted wind tunnel tests utilizing PIV (particle image velocimetry) technology to investigate how various roof angles impact the airflow patterns surrounding a gable-roof structure. The researchers discovered that the diversity of roof inclinations had an impact on the swirling pattern within the area behind the model. Zhong M. [14,15] analyzed the wind pressure distribution of a low-rise building model in three typical mountain terrains along coastal areas with a wind tunnel test.

Mostafa et al. [16] analyzed proportional models with different geometric parameters through wind tunnel tests and concluded that the width of the eaves affects the magnitude of the pressure coefficient, which needs to be considered in the design process. Abdlfatah et al. [17] used the CFD method to study two models of single-story buildings and two-story gable walls. In different heights of stilts, the relationship between the reference height and the roof pressure coefficient should be considered. R.H. Ong et al. [18] conducted computational fluid dynamics (CFD) analysis on low-rise buildings immersed in turbulent boundary layers. The study focused on the impact of incident turbulence intensity and grid size on the flow around the SilSOE 6 m cube in eight sub-grid scale (SGS) models. The influence of the above factors on the first-order statistics of the pressure coefficient is limited, but their influence becomes more pronounced when analyzing high-order statistics (i.e., variance, skewness, and kurtosis) and extreme values. Ye Qiu et al. [19] combined optimization algorithms with computational fluid dynamics (CFD) simulations, based on four turbulence closure models (standard k-ε, RNG k-ε, and SST k-ω). For the first time, the performance of solid parapet walls in reducing flat roof suction induced by conical vortices was studied in conjunction with RSM. CFD-based automatic optimization methods were used to find the best-performing porosity. A porous parapet wall with an optimal porosity between 38.2% and 52.3% seems to be more effective than a solid parapet wall in attenuating the high angle suction generated by conical vortices. However, when $hp/H \geq 0.07$, solid parapets perform best in reducing wind suction. A. Jameel et al. [20] conducted a comprehensive numerical study of wind effects on low-rise buildings using computational fluid dynamics (CFD) techniques, using the standard k-ε turbulence models and renormalization groups. k-ε turbulence models are used to predict wind loads and flow patterns around ridge buildings. The wind pressure coefficient calculated above compared the roof and wind tunnel data of a sloping roof building. The results obtained using RNG were found to be consistent with the standard k-ε. Compared to turbulence models, the k-ε turbulence model matches well with wind tunnel data. Ryan Honerkamp et al. [21] established a numerical model of a physical tornado simulator through computational fluid dynamics (CFD) simulation and verified the blunt body aerodynamic characteristics of buildings under the action of tornadoes through measurement data of building models tested in a physical tornado simulator. Hnaien et al. [22] considered a computational fluid dynamics (CFD) model based on steady-state Reynolds-averaged Navier–Stokes equations (RANSs) using k-ω. Two equation turbulence models were used to estimate the airflow distribution around buildings. We studied the wind comfort of pedestrians in urban areas and confirmed that weather conditions (wind speed and direction) and building layout are key parameters of comfort. Sharma et al. [23] conducted numerical research using ANSYS CFX, combining a k-value model with a scale of 1:50. A turbulence model was used to discover the wind-induced effects of cylindrical roofs in low-rise buildings by arranging them in a rectangular pattern with variable spacing (i.e., 100, 200, 300, and 400 mm) and 15° intervals. The interval bears different wind attack angles (AoA). The results indicated that the windbreak effect plays a crucial role in reducing the wind-induced effects of upstream buildings on interfering buildings. Singh et al. [24,25] used CFD to simulate the pressure distribution on pentagonal and hexagonal cone roofs and compared the pressure coefficients on building models with and without openings. They found that the pressure coefficient on hexagonal cone roofs was lower, whereas the pressure coefficient on unopened building models was twice or three times that of open building models.

Current research mainly focuses on analyzing the influence of structural parameters and relative positions between building clusters on the wind load of low-rise buildings, while ignoring the influences of mountain terrain. Due to the significant influences of pulsating wind pressure characteristics on the surface of low-rise buildings, it is necessary to study the pulsating wind pressure characteristics of low-rise buildings at different spacings. This paper conducts a comprehensive investigation into the impact of altering the relative position of the building and the mountain of the double-slope roof structure.

## 2. Wind Tunnel Test Experiments

Wind tunnel tests were conducted at the Department of Civil Engineering at Hunan University. The working section has a width of 3.0 miles, a height of 2.5 miles, and a length of 10 miles.

### 2.1. Full-Sized Physical Model

Simulating the atmospheric boundary layer involves representing it as a geometric scale of 1:40. As shown in Figure 2, the design of the building's physical-scale model is derived from the prevalent low-rise structures found in China. The dimensions of the actual mountain model are determined by the specifications outlined in the Load code for the design of building structures (GB50009-2012) [26], which includes guidelines for constructing a low-rise building situated close to a mountain.

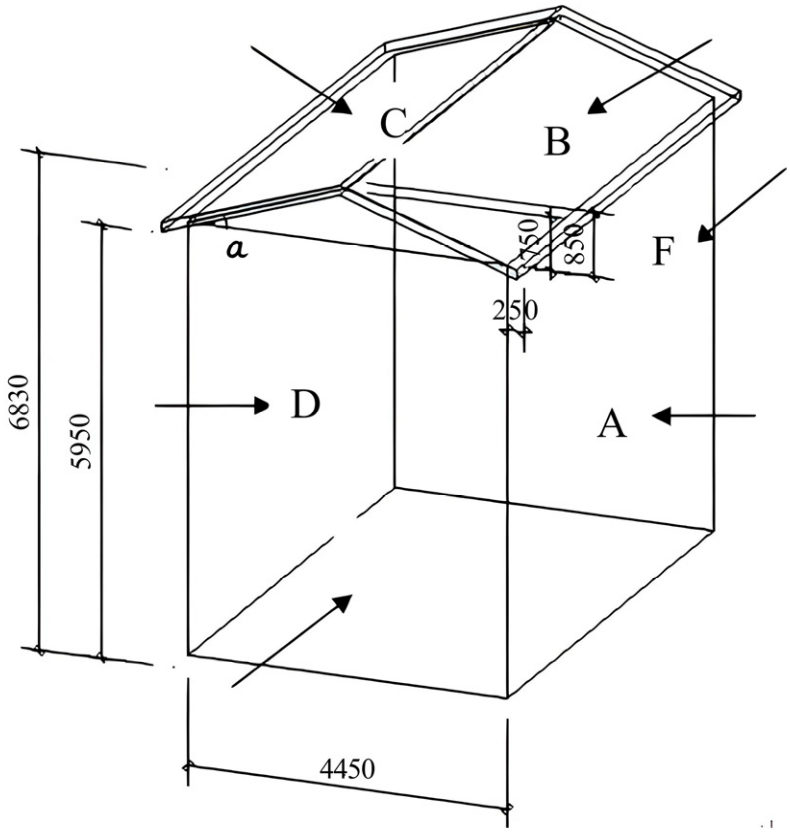


**Figure 2.** Dimensions of the model of the low-rise buildings (units: mm).

A 1:40 scale model of a building was constructed to depict a structure measuring 6.83 m high (H), 4.45 m wide (W), and 7.5 m long (L). The roof had an extension of 0.25 m from the side of the building. Testing points for pressure taps can be found on walls, roofs, and both sides of the eaves. The total number of testing points is 374, with 202 on the walls, 130 on the roof, and 42 on the eaves. The pressure testing points are shown in Figure 3.

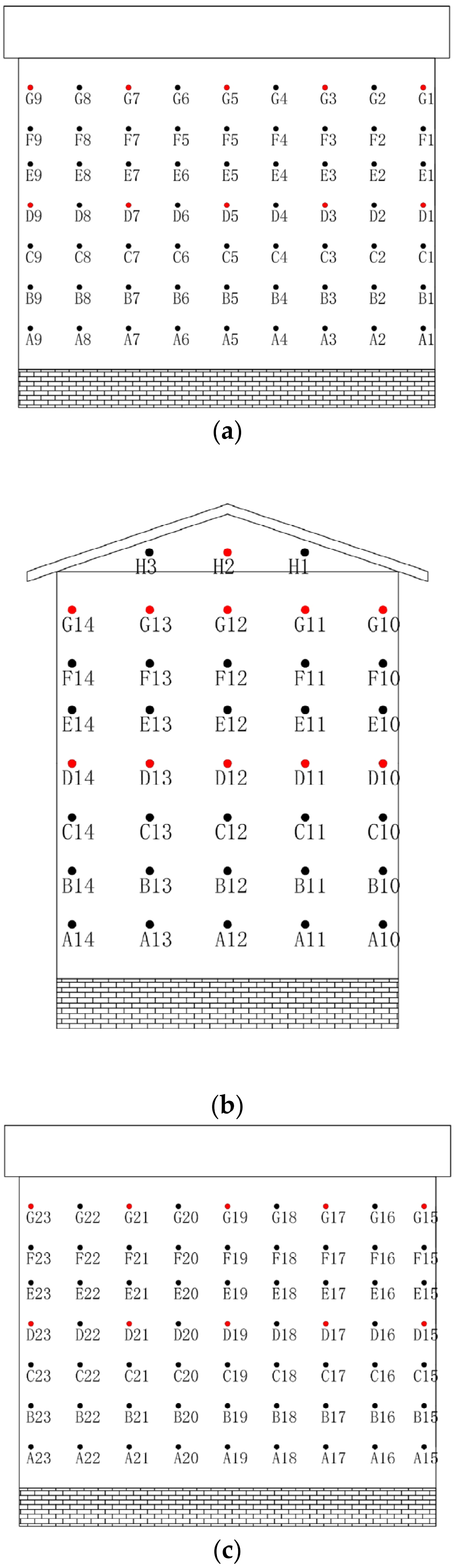


**Figure 3.** *Cont.*

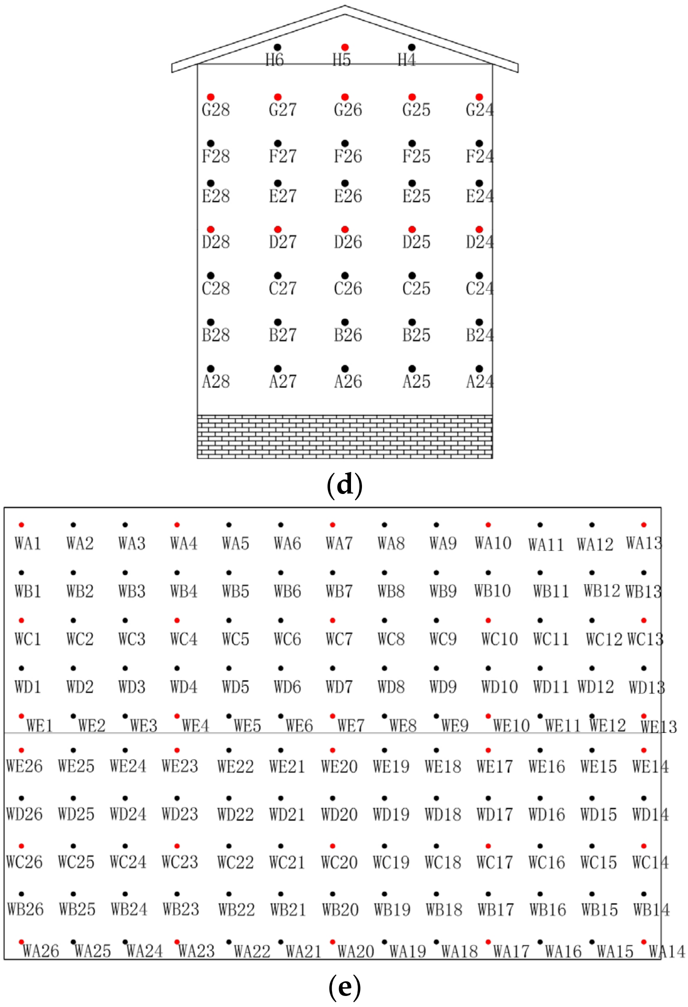


**Figure 3.** Measurement point distribution: (**a**) layout of A-side measuring points; (**b**) layout of E-plane measuring points; (**c**) layout of D-side measuring points; (**d**) layout of F-plane measuring points; (**e**) layout of roof measurement points.

### 2.2. Experimental Operating Conditions

Figure 4 shows the position of the experimental model and the mountain. The low-rise building's height is represented by $H$, and the hillside height is represented by $H_{\mathrm{m}}$. The hillside slope is represented by $\beta$, and the roof slope is represented by $\alpha$. The distance between the hillside and the house is represented by $S$. In the experiment, the angle of wind was tested from 0° to 90° with a 5° interval, as depicted in Figure 5. The hillside without surroundings has been considered to analyze the wind pressure affected by the distance between the hillside and the house. Table 1 displays the specifics of the parameters. Because the wind speed in the wind tunnel test does not affect the fluctuating wind pressure coefficient and its characteristics, we selected a wind speed of 12 m/s at level 6 with moderate wind speed as the wind speed for the wind tunnel test. Considering that the blockage rate of the overall model in the wind tunnel test room cannot exceed 5%, we choose 1:40 as the geometric scaling ratio of the wind tunnel test model. The wind tunnel experiment meets all the necessary criteria for the blocking probability. This experiment uses the DSM3400 electronic pressure scanning valve system from Scanivalve, an American scanning valve company, to collect and process wind pressure data. The wind pressure acquisition system consists of a pressure-measuring tube on the surface of the model, a pressure conduit, a pressure sensor, a signal acquisition and processing program, etc. Each scanning valve acquisition module can connect 64 measurement points, and the acquisition system can connect eight pressure scanning valve acquisition modules with a sampling frequency of 312.5 Hz.

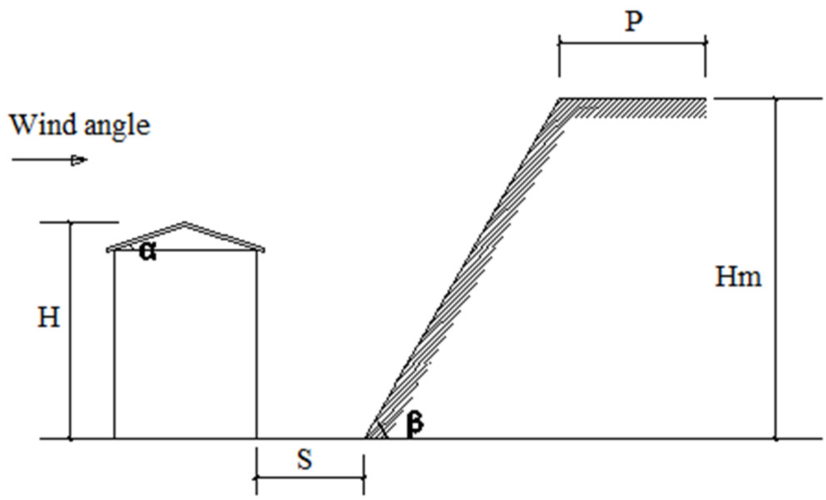


**Figure 4.** Position of schematic diagram of the experimental model mountain.

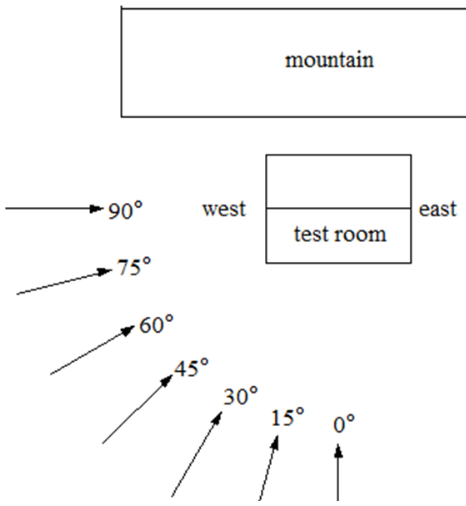


**Figure 5.** Wind direction.

**Table 1.** Detailed information on experimental parameter studies.

| | | |
|---|---|---|
| **Model size** | Length of the model | 187.5 mm |
| | Width of the model | 111.25 mm |
| | Slope of the roof | 18.6° |
| **Relative position of the mountain** | Distance | 34.15 mm ($S/H$ = 0.2)<br>68.30 mm ($S/H$ = 0.4)<br>170.75 mm ($S/H$ = 1.0) |
| | Mountain height $H_m$ | 34.15 mm ($H_m/H$ = 2) |
| **Slope of the mountain, $\beta$** | 60° | |
| **Terrain roughness, $z_0$** | 0.12 | |
| **Sampling frequency of the wind pressure** | 312.5 Hz | |
| **Tunnel velocity** | 12 m/s | |
| **Geometric scale ratio** | 1:40 | |

To calculate the dimensionless wind pressure coefficient at the measurement point, according to the calculation formula of the wind pressure coefficient, it is necessary to set a reference point for wind speed. The dynamic pressure at the measurement point is divided by the dynamic pressure at the reference point to obtain the wind pressure coefficient. To ensure that the reference point does not affect the pressure measurement of the model itself and can reflect the incoming flow characteristics at the model location well, this experiment considers setting the reference point 50 cm above the ground, corresponding to a real prototype wind field height of 20 m.

Preliminary research has found that under a slope of 60°, the wind pressure distribution characteristics and pulsating wind pressure characteristics on the surface of low-rise houses are more stable and have more obvious patterns. Therefore, we chose a relatively more common and representative slope of 60°.

### *2.3. Testing the Simulation of Wind Patterns*

#### 2.3.1. Wind Profile of the Test Wind Farm

Research has shown that using logarithmic law to represent wind profiles within an extended height range is relatively satisfactory. However, in the field of structural engineering, for convenience, China's load regulations usually use exponential rates to describe wind profiles. The expression for wind profiles is

$$v_z = v_{10}\left(\frac{z}{10}\right)^{\alpha} \tag{1}$$

Among them, the index $\alpha$ represents the ground roughness index, and Class A and B wind fields are taken as 0.12 and 0.15, respectively. In wind tunnel tests, to simulate turbulent atmospheric boundary layers with wind profile indices of 0.12 and 0.15, simulation devices such as baffles, spires, and rough elements are usually used.

#### 2.3.2. Turbulence Profile of Experimental Wind Field

Turbulence is the ratio of the standard deviation of fluctuating wind speed to the average wind speed, reflecting the intensity of wind fluctuation and playing a crucial role in determining the wind load on the structure. Assuming that at height z, the time series of wind speeds corresponding to moments $t_1$, $t_2$, $t_3$, and so on is $v_1$, $v_2$, $v_3$, and so on, respectively, the average wind speed $v_0(z)$ throughout this wind speed time history is:

$$v_0(z) = \frac{1}{n}\sum_{t=1}^{n} v_t(z) \tag{2}$$

The standard deviation of wind speed at height $z$ is denoted as $\sigma(z)$.

$$\sigma(z) = \left(\frac{1}{n}\sum_{t=1}^{n} v_t(z) - v_0(z))^2\right)^{\frac{1}{2}} \tag{3}$$

The turbulence intensity at height $z$ is $I_z(z)$.

$$I_z(z) = \frac{\sigma(z)}{v_0(z)} \tag{4}$$

According to the provisions of the Load code for the design of building structures (GB50009-2012) in China regarding turbulence intensity, the calculation formula for height distribution is as follows:

$$I_Z(Z) = I_{10}\bar{I}_Z(Z) \tag{5}$$

$$I_Z(Z) = I_{10}\left(\frac{z}{10}\right)^{-\alpha} \tag{6}$$

In the above equation, $I_{10}$ represents the turbulence level at a height of 10 m.

To create a comparable setting in regular mountainous landscapes, a wind velocity of 12 m/s is established. This can be replicated in wind tunnel experiments by incorporating triangular structures and ground roughness components with a power exponent of 0.12 to simulate natural wind conditions. Figure 6 displays the experimental models and setup for the wind tunnel tests in the simulation. Figure 7 illustrates the profiles of mean wind speed and turbulence intensity. In the experiment, landforms A were achieved by using binary spires, baffles, and rough elements. The specific situation of the inflow wind field of two types of landforms A simulated according to specifications in wind tunnel tests is shown in Figure 6. Figure 7 shows the average wind speed profile and turbulence intensity profile of the rough category A wind field obtained according to the above arrangement in the wind tunnel.

**Figure 6.** Wind field layout.

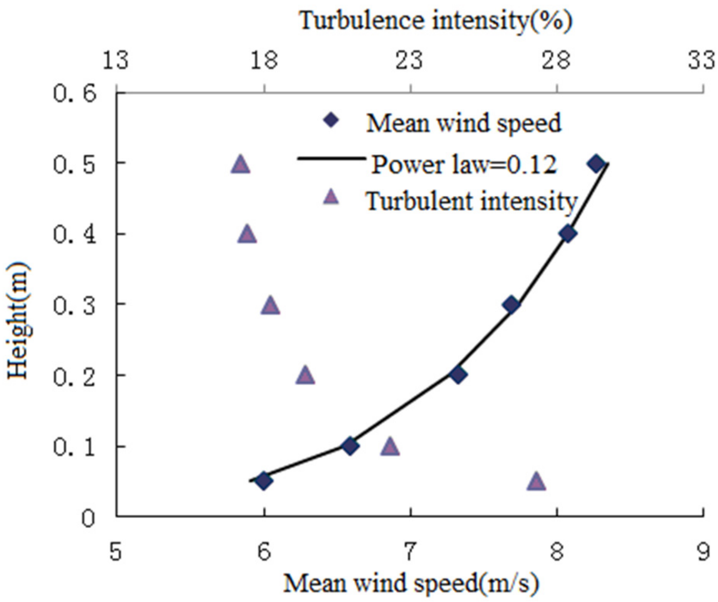


**Figure 7.** Profile of wind velocity and turbulence.

### 2.4. Method of Analyzing Data

Mean Wind Pressure Coefficient

The formula for expressing the average wind pressure coefficient is as follows:

$$C_p = \frac{p_i - p_0}{\frac{1}{2}\rho U_r^2} \tag{7}$$

The static (ambient, atmospheric) reference pressure, denoted as $p_0$, is determined based on the wind tunnel test's reference height (0.4 m), which is equivalent to a realistic height of 40 m. The mean velocity is denoted as $U_r$, and the air density is denoted as $\rho$; this in turn determines the instantaneous surface pressure, represented as $p_i$.

The fluctuating wind pressure coefficient is defined as follows:

$$C_{p,rms} = \frac{1}{N}\sqrt{\sum_{i=1}^{N}(C_p(t_i) - C_{p,mean})^2} \tag{8}$$

According to Figure 8, it can be seen that when *S/H* = 0.2, the fluctuating wind pressure coefficient shows a trend of first decreasing and then increasing from top to bottom along the height direction of the windward surface. The maximum value occurs near the eaves at the upper part, with a value of 0.14. When *S/H* = 0.4, the fluctuating wind pressure coefficient increases, with a maximum value of 0.142. When *S/H* = 1.0, the fluctuating wind pressure coefficient continues to increase, with a maximum value of 0.148. As the distance between the slope and the mountain increases to infinity, when there is no surrounding environmental impact, the pulsating wind pressure coefficient slightly decreases, with a maximum value of 0.144. It can be seen that when the distance between the slope and the mountain increases, the pulsating wind pressure coefficient at the windward side shows a trend of first decreasing and then increasing.

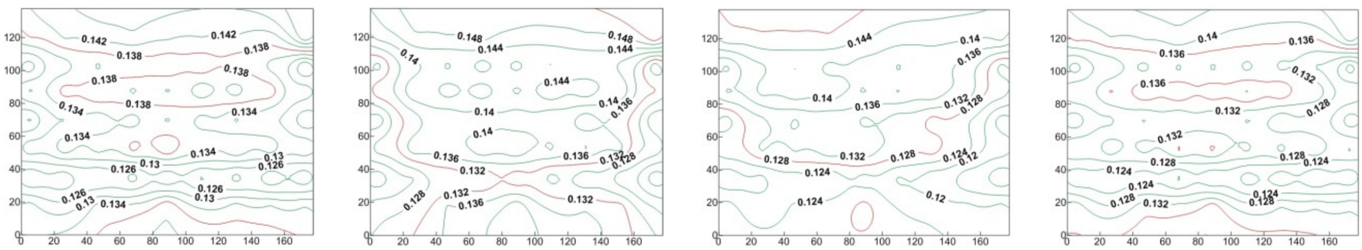

(**a**) *S*/*H*=0.2 (**b**) *S*/*H*=0.4 (**c**) *S*/*H*=1.0 (**d**) no periphery

**Figure 8.** Contour map of average wind pressure coefficient on the windward side.

As shown in Figure 9, when *S/H* = 0.2, the fluctuating wind pressure coefficient gradually increases from top to bottom along the height direction, with a maximum value of 0.17, appearing at the corner near the leeward surface. When *S/H* = 0.4, there is no significant change in the wind pressure distribution, and the fluctuating wind pressure coefficient increases, with a maximum value of 0.19. When *S/H* = 1, the maximum value of the fluctuating wind pressure coefficient is 0.205. When *S/H* approaches infinity, and there is no influence from the surrounding environment, the distribution of the fluctuating wind pressure coefficient changes significantly compared to when there is a surrounding area. The maximum value occurs near the windward surface and the eaves, with a value of 0.185.

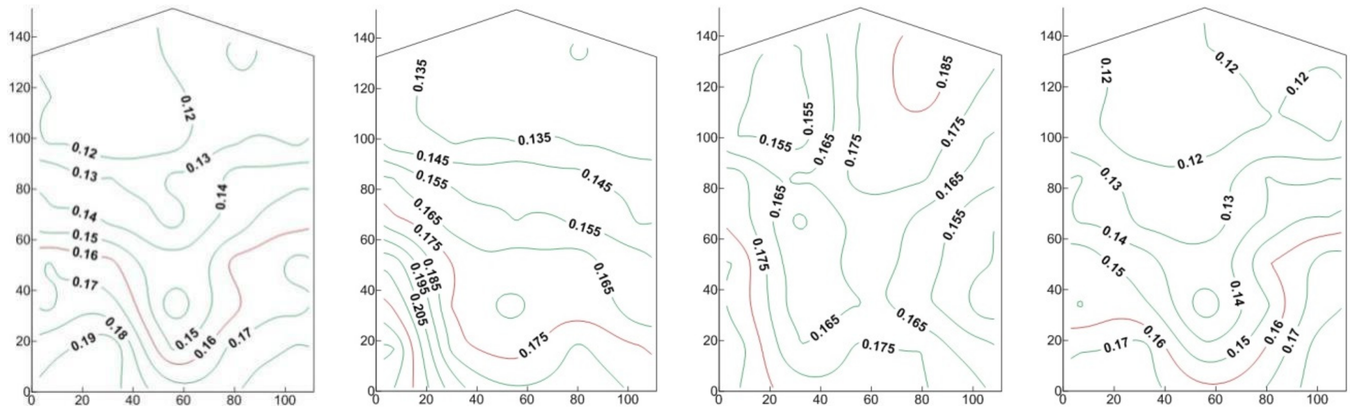

(**a**) $S/H$=0.2 (**b**) $S/H$=0.4 (**c**) $S/H$=1.0 (**d**) no periphery

**Figure 9.** Contour map of average wind pressure coefficient on the left side.

From Figure 10, it can be seen that when *S/H* = 0.2, the fluctuating wind pressure coefficient gradually increases from top to bottom in the height direction, with a maximum value of 0.146. When *S/H* = 0.4, the fluctuating wind pressure coefficient value increases, with a maximum value of 0.15. When *S/H* = 1, the fluctuating wind pressure coefficient value continues to increase, with a maximum value of 0.165. When the spacing continues to increase to infinity, the distribution state changes significantly compared to when there is a mountain, and the fluctuating wind pressure coefficient gradually decreases from the surrounding area to the center, with a minimum value of 0.087.

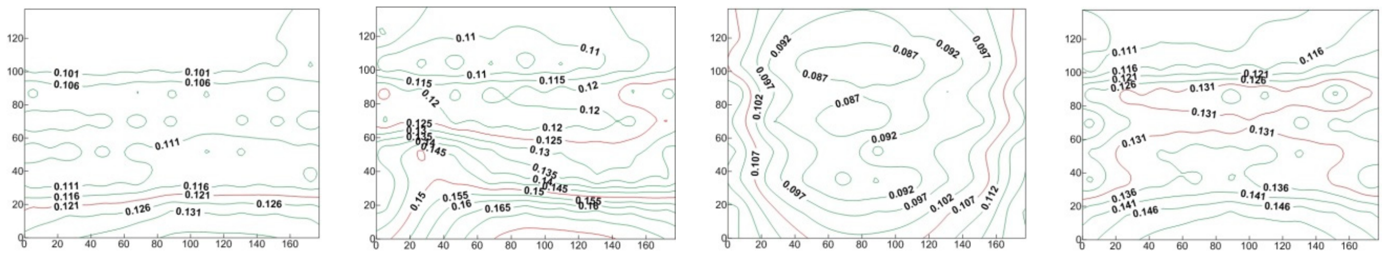

(**a**) $S/H$=0.2 (**b**) $S/H$=0.4 (**c**) $S/H$=1.0 (**d**) no periphery

**Figure 10.** Contour map of the average wind pressure coefficient on the leeward side.

As shown in Figure 11, when *S/H* = 0.2, the fluctuating wind pressure coefficient gradually increases from top to bottom along the height direction, with a maximum value of 0.165. When *S/H* = 0.4, the fluctuating wind pressure coefficient increases, with a maximum value of 0.19. When *S/H* = 1, the fluctuating wind pressure coefficient continues to decrease, with a maximum value of 0.155, appearing near the leeward surface at the bottom. When the spacing continues to increase to infinity, the fluctuating wind pressure coefficient increases, especially in the area near the roof, with a maximum value of 0.175.

According to Figure 12, when *S/H* = 0.2, the fluctuating wind pressure coefficient of the roof has a maximum value of 0.18 at the windward eaves. When *S/H* = 0.4, the distribution of the fluctuating wind pressure coefficient remains unchanged. When *S/H* = 1, the fluctuating wind pressure coefficient increases, with a maximum value of 0.19. As the distance between the mountain slope and the mountain body continues to increase, the fluctuating wind pressure coefficient continues to increase, and the contour lines of wind pressure distribution are relatively denser compared to when there are mountains. The maximum value of the fluctuating wind pressure coefficient is 0.22, which appears at the windward roof.

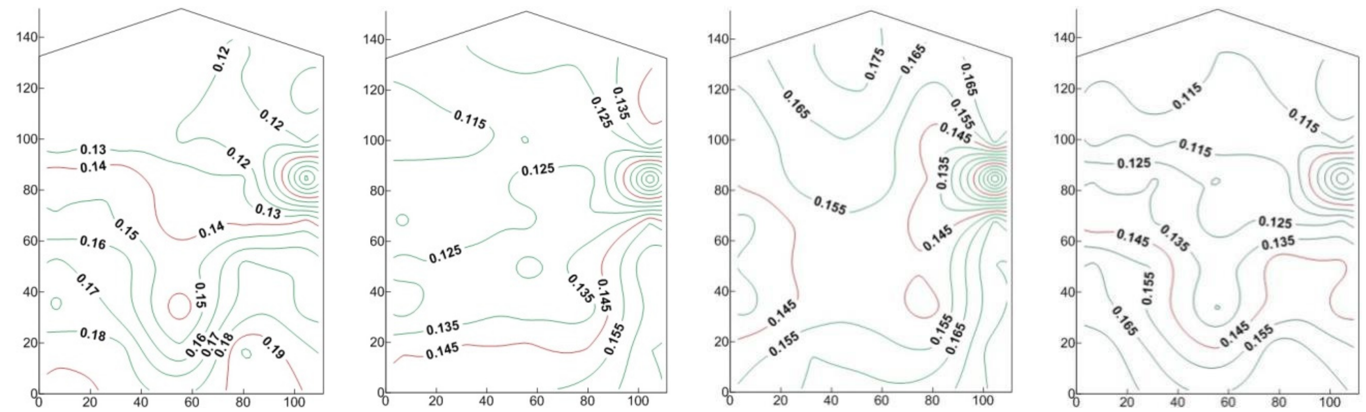

(**a**) $S/H$=0.2 (**b**) $S/H$=0.4 (**c**) $S/H$=1.0 (**d**) No periphery

**Figure 11.** Contour map of average wind pressure coefficient on the right side.

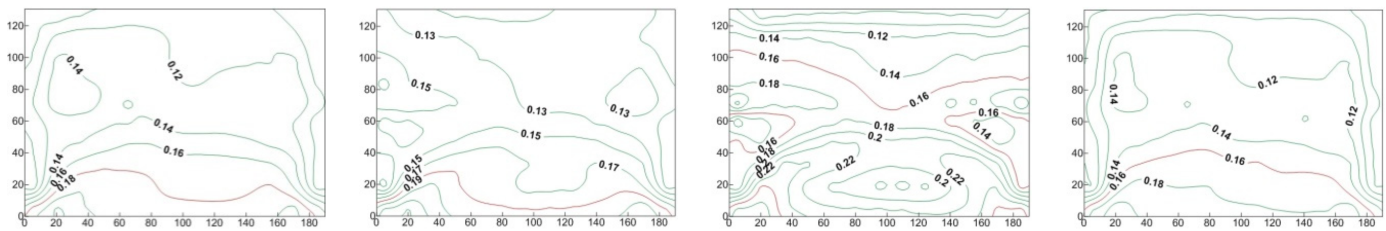

(**a**) $S/H$=0.2 (**b**) $S/H$=0.4 (**c**) $S/H$=1.0 (**d**) No periphery

**Figure 12.** Contour map of average roof wind pressure coefficient.

## 3. Fluctuating Wind Pressure's Interference Effect

To analyze the change law on the fluctuating wind pressure coefficient at crucial measurement locations with the space between the hillside and the structure, the variation in the mean wind pressure coefficient at different measuring points with varying slope heights is analyzed. Figure 13 shows the layout of selected representative measurement points. Figure 14a reveals that in the middle of the windward side, the fluctuating coefficient exceeds the coefficient at the edge measuring points.

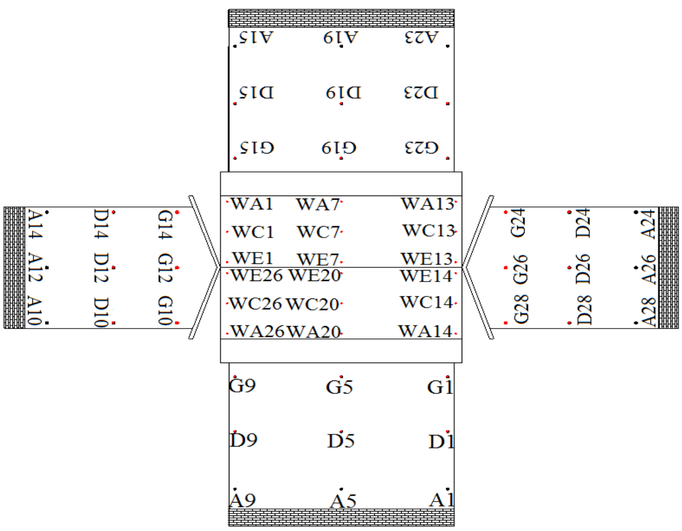


**Figure 13.** Key point location.

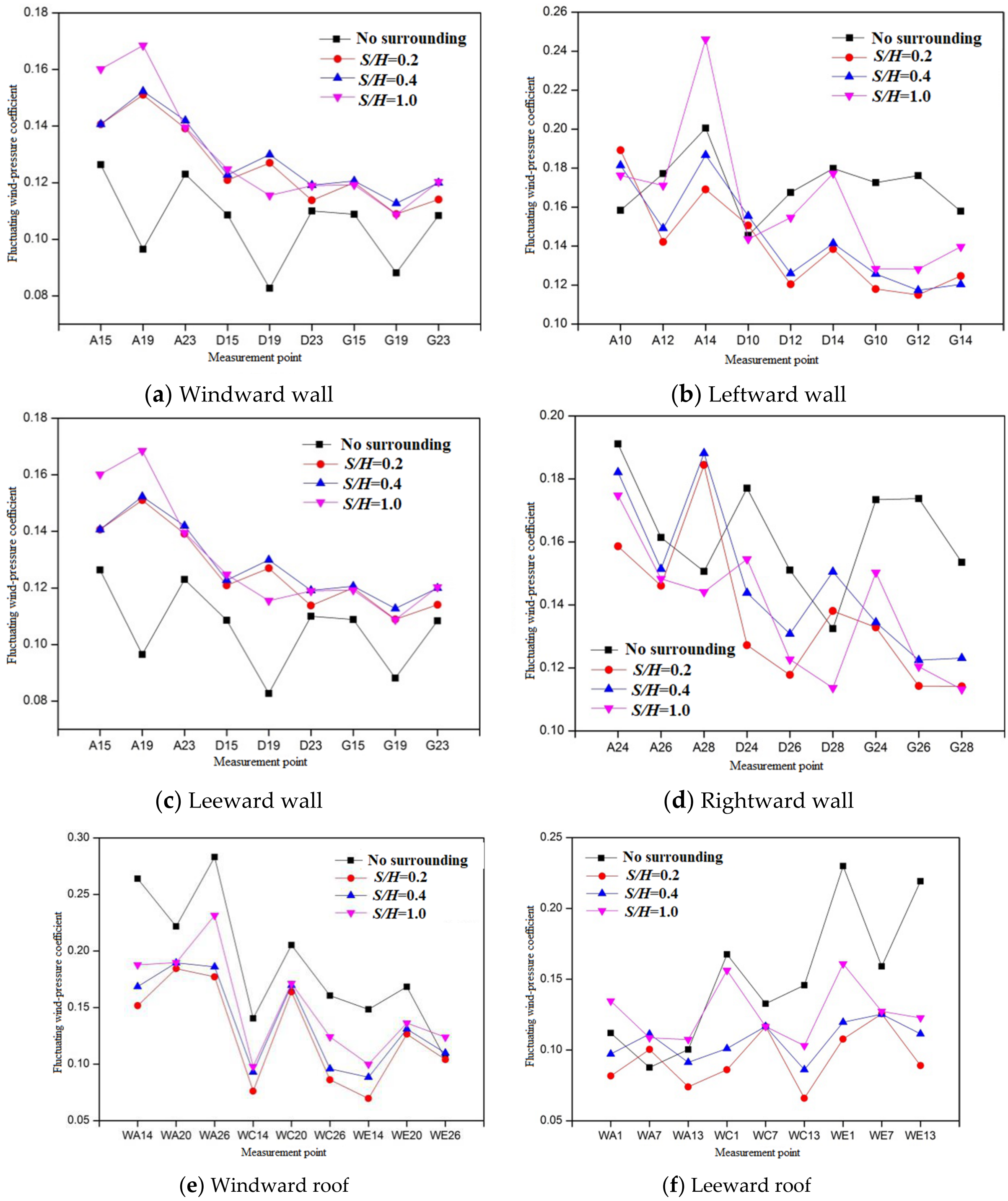


(**a**) Windward wall (**b**) Leftward wall

(**c**) Leeward wall (**d**) Rightward wall

(**e**) Windward roof (**f**) Leeward roof

**Figure 14.** The measuring point's fluctuating wind pressure coefficient.

Additionally, compared to A5, A1 experiences a 13.5% decrease in its fluctuating coefficient. The fluctuating coefficient of G5 and G9 is smaller than that of G1, and it exhibits a rising pattern. However, when there is a hillside, G1, G5, and G9 demonstrate a declining pattern.

Compared to the measuring point at the edge, the fluctuating coefficient is lower at the middle line. The fluctuating coefficient of A14 is 0.246, which is 43.8% higher than that of A12.

According to Figure 14c, in the absence of any impact from the surrounding environment, the fluctuating wind pressure coefficient at the middle line measuring point is lower compared to the edge. However, in the presence of a mountain, the fluctuating coefficient at the middle line is higher than that on the margins.

The information depicted in the diagram is evident in Figure 14d. A24, D24, and G24 have the largest values in the same row of measurement points when there is no periphery in working conditions 1 and 2. In working condition 3, the fluctuating coefficient at A26 is higher than that at A24. Similarly, in rows D and G, the edge measuring points D24 and G24 have a greater fluctuating wind pressure coefficient than the other measuring points in their respective rows.

The absence of a clear correlation between the fluctuating coefficient of the mid-line and the edge measuring point can be observed in Figure 14e when the windward roof remains unaffected by the surrounding environment. In general, the fluctuating coefficient of the windward roof is higher than that without the surrounding environment.

Additionally, measuring points located along the middle line exhibit a lower fluctuating coefficient compared to measuring points situated at the edge when considering different mountain spacing.

Figure 14f illustrates that the middle measuring point's fluctuating coefficient is lower than that on the margins when the leeward roof remains unaffected by the surrounding environment. The fluctuating coefficient at the middle measuring point exhibits less variation compared to the edge measuring point when a mountain is present. Notably, the value at measuring point WE7 remains constant.

## 4. Examining the Fluctuating Coefficient under Different Wind Angles

When the wind direction is between 60° and 80°, the fluctuating coefficients are at their lowest, unaffected by the surrounding environment. Then, $S/H$ = 0.4, $S/H$ = 0.2, and finally, $S/H$ = 1.0. When the wind direction ranges from 85° to 90°, the fluctuating wind pressure coefficient increases when the distance increases, and the difference in the fluctuating coefficient is minimal.

In Figure 15b, the maximum fluctuating coefficient is 0.21 when the wind direction is 15°. At a wind direction of 70° and a ratio of $S/H$ equal to 0.4, the highest coefficient for fluctuating wind pressure is 0.22. As the wind angle increases, the fluctuating coefficient initially rises, then falls, and ultimately rises when the working condition $S/H$ = 1.

The fluctuating coefficient of measuring point D19 in the middle of the leeward side is reduced in the absence of any impact from the surrounding environment, as depicted in Figure 15c. The mountain's fluctuating wind pressure coefficient does not follow a clear rule under three different spacing conditions.

The fluctuating coefficient remains approximately 0.08 when the wind direction ranges from 35° to 90°, as shown in Figure 15d. The fluctuating wind pressure coefficient values under $S/H$ = 0.2 are similar to those under $S/H$ = 0.4, and both values decrease gradually with the increase in wind direction increase. As the wind direction increases, the fluctuating coefficient initially rises, then falls, and eventually rises again when the working condition is $S/H$ = 1.0. At a wind direction of 20°, the highest fluctuating coefficient is 0.135.

The wind pressure coefficient at the windward eave is lower in the absence of surrounding environmental influence compared to when there is a mountain, as depicted in Figure 15e. As the wind direction rises to 75°, the fluctuating wind pressure coefficient accelerates and reaches a peak value of 0.18 under the wind direction of 90°.

As is shown in Figure 15e, at a wind direction of 60°, the minimum fluctuating coefficient is 0.122. In the presence of a peak, with a ratio of $S/H$ equal to 1.0, when the wind blows at an angle of 75°, the fluctuating coefficient reaches its highest point at 0.25.

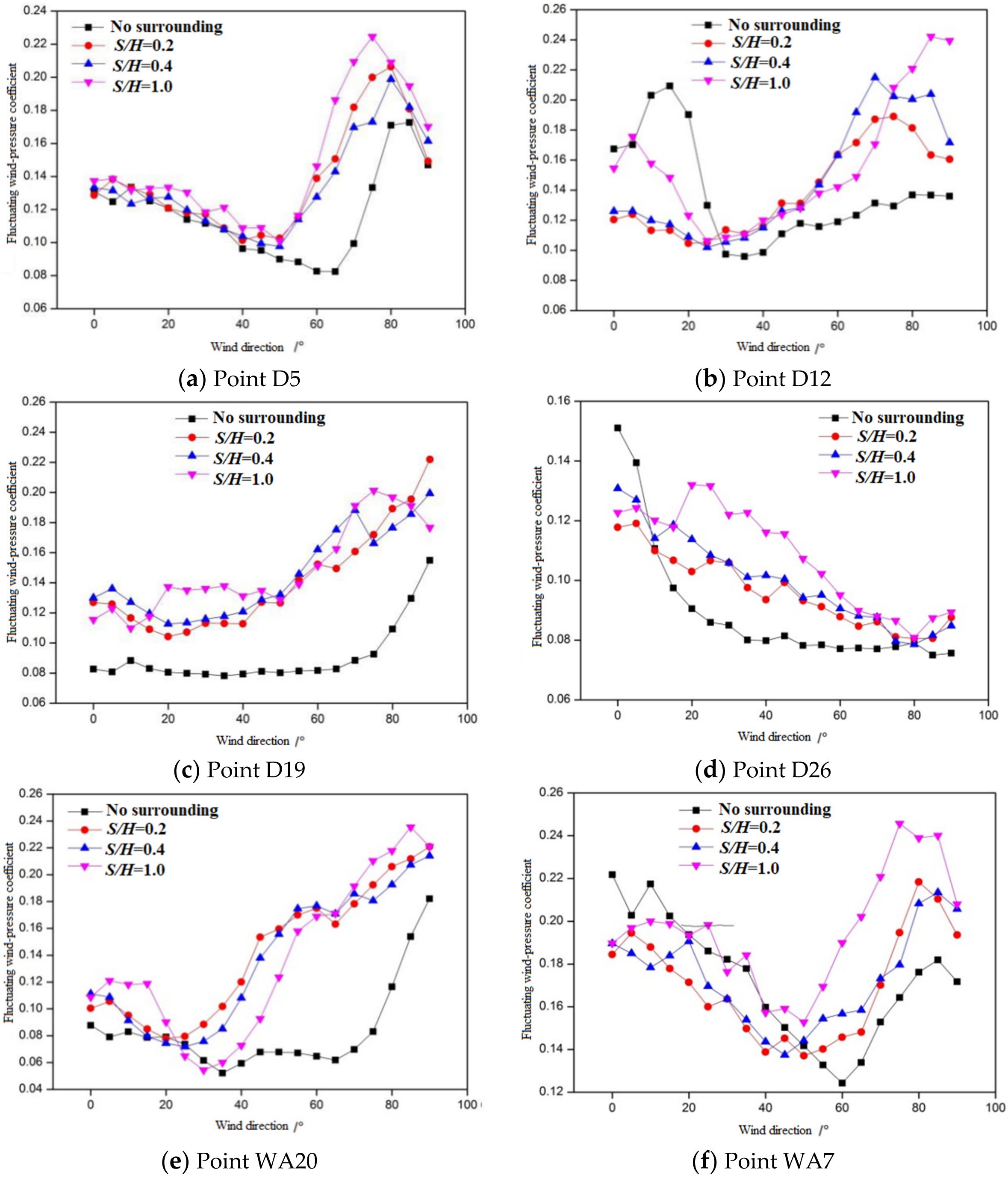


(**a**) Point D5 (**b**) Point D12

(**c**) Point D19 (**d**) Point D26

(**e**) Point WA20 (**f**) Point WA7

**Figure 15.** The fluctuating coefficient at the representative measuring point.

## 5. Comparative Analysis of the Power Spectrum

The wind load usually acting on building structures consists of two parts: average wind and pulsating wind. Therefore, the structural wind load action is divided into static and dynamic under average wind influence. The static method can be used to calculate the effect of average wind. However, due to the randomness of pulsating wind, the random vibration theory is generally used to analyze the structural vibration caused by pulsating wind.

From the perspective of the frequency domain, an effective way to explore the characteristics of pulsating wind pressure is to study its pulsating wind pressure spectrum. The pulsating wind pressure of low-rise buildings is relatively complex, and the pulsating wind pressure spectrum of measurement points is usually influenced by various factors such as wind direction angle, measurement point position, structural size, roof shape, incoming turbulence, etc. To comprehensively analyze the pulsating wind pressure characteristics of low-rise buildings, this chapter compares and analyzes the power spectra of representative measurement points and pulsating wind pressure under different parameters from the perspective of the frequency domain and explores the pulsating wind pressure characteristics of low-rise buildings.

The power spectra in the following figure are all normalized power spectra, with the x-axis representing the reduced frequency and the y-axis representing the dimensionless self-spectral function $S^* = \frac{fS(f)}{\sigma^2}$; $B$ is the model width; $V_z$ is the wind speed at the reference point height, which is the same as in Section 2; $S(f)$ is the wind pressure self-power spectral function at the measurement point; $\sigma^2$ is the variance of wind pressure at the measurement point. The vortex turbulence characteristics caused by the structural surface, also known as characteristic turbulence [27], and the longitudinal pulsating wind pressure turbulence characteristics related to the characteristics of the incoming wind are the two main factors affecting the pulsating wind pressure of low-rise buildings.

Figure 16 shows that at a wind direction of 0°, the spectral peak on the windward direction is distinct, measuring approximately 0.76. That occurs when the reduction frequency of the low-frequency band is 0.08 and when there is no surrounding building. The energy in the high-frequency band is minimal, with the majority of energy concentrated in the low-frequency range, primarily within the expansive vortexes in space. Typically, the maximum amplitude of the distinct spectral peak in the high-frequency band is enhanced following an increase in the elevation of the mountain. The findings indicate that the presence of the mountain alters the flow, leading to an augmentation in small-scale vortices and an elevation in high-frequency band energy. As the hillside and the building move further apart, the maximum value of the spike spectral peak in the low-frequency band gradually rises, and the energy of the large-scale vortex steadily grows.

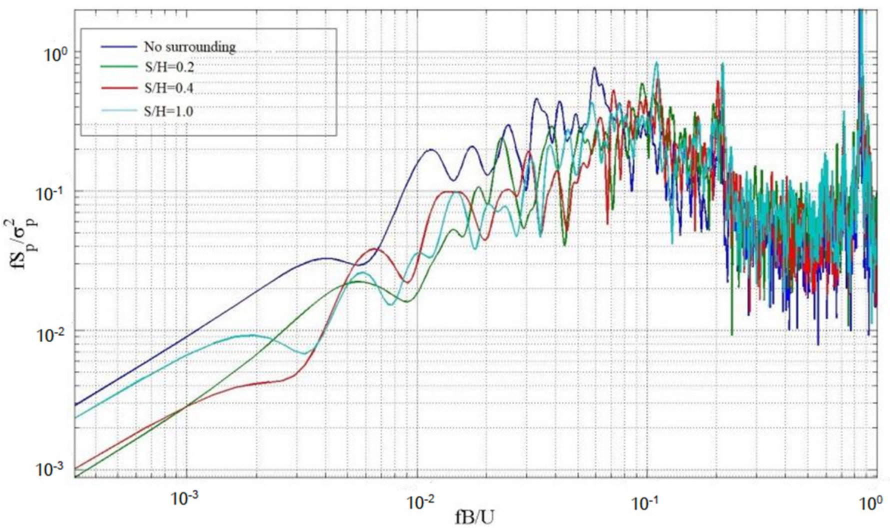


**Figure 16.** The power spectrum analysis at D5.

Figure 17 shows that the spectrum is abundant in the low-frequency range when D12, under a wind direction of 0°, has no impact on the surrounding environment. At a reduction frequency of 1.2 for the high-frequency range, a distinct spectral peak emerges with a peak value of approximately 0.65, and the energy of the remaining high-frequency range is minimal. The presence of the mountain alters the low-frequency band's spectrum from wide to narrow, and the high-frequency band's spectral peak rises in comparison to when the surrounding environment has no impact. This suggests that the mountain's existence causes an increase in energy in the middle of the left side within the high-frequency range.

Additionally, the small-scale vortex and large-scale vortex experience slight increases when compared to the absence of the surrounding environment's influence.

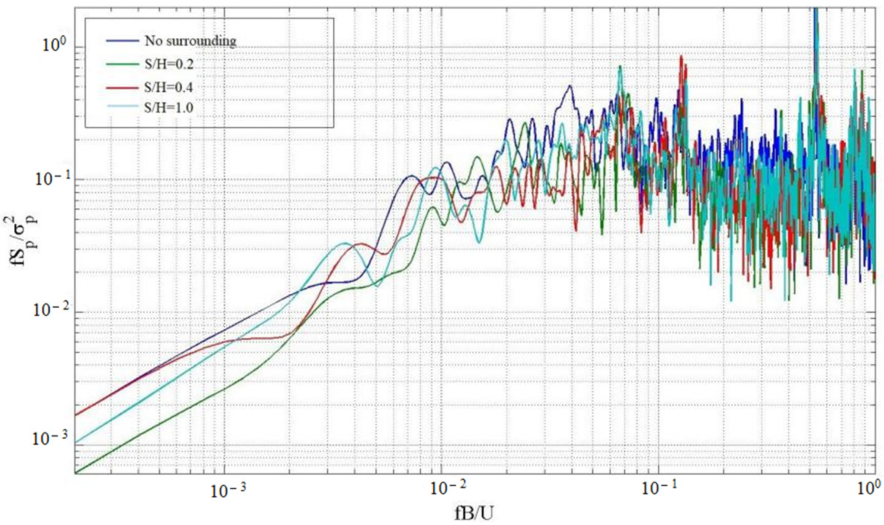


**Figure 17.** The power spectrum analysis at D12.

Figure 18 illustrates that when there is a mountain under the wind direction of 0°, the spectral peak value of the high-frequency band decreases on the leeward side, unaffected by the surrounding environment. As the hillside and the building move further apart, the spectral peak value of the low-frequency band steadily rises. On the other hand, there is a decrease in the maximum value of the high-frequency spectral band. The data indicate a gradual shift in energy from a higher frequency to a lower frequency. Additionally, the impact of fluctuating wind pressure, resulting from the incoming wind's characteristics, becomes more pronounced, and the effect of vortex turbulence caused by the mountain diminishes.

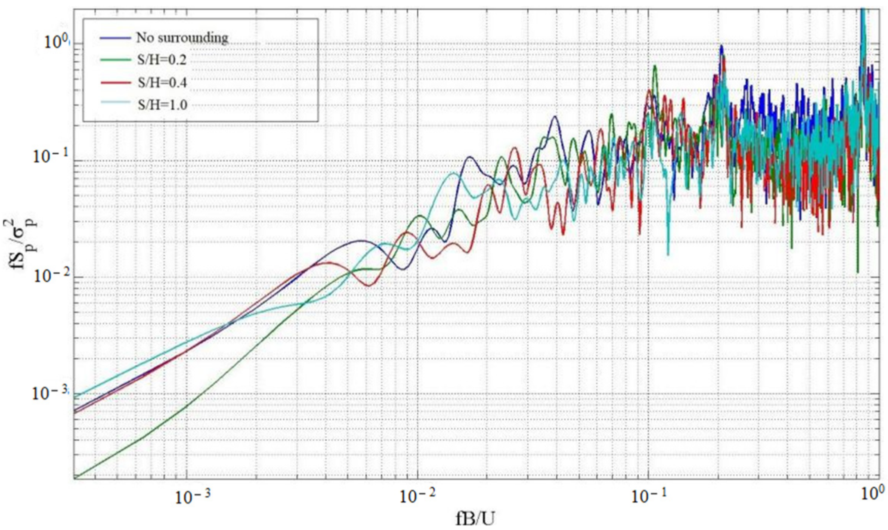


**Figure 18.** Power spectrum analysis at D19.

Figure 19 shows that when $S/H$ = 0.2, the low-frequency band's spectral peak value at D26 decreases, and the high-frequency band's spectral peak value increases relatively on the right side, unaffected by the surrounding environment. Currently, the energy frequency moving from low to high leads to a reduction in the impact of the fluctuation, resulting from the properties of the incoming wind. Nevertheless, the impact of the vortex turbulence resulting from the mountain formation escalates. As the hillside and the building move further apart, the high-frequency energy gradually diminishes, leading to a weakening of the vortex turbulence caused by the mountain.

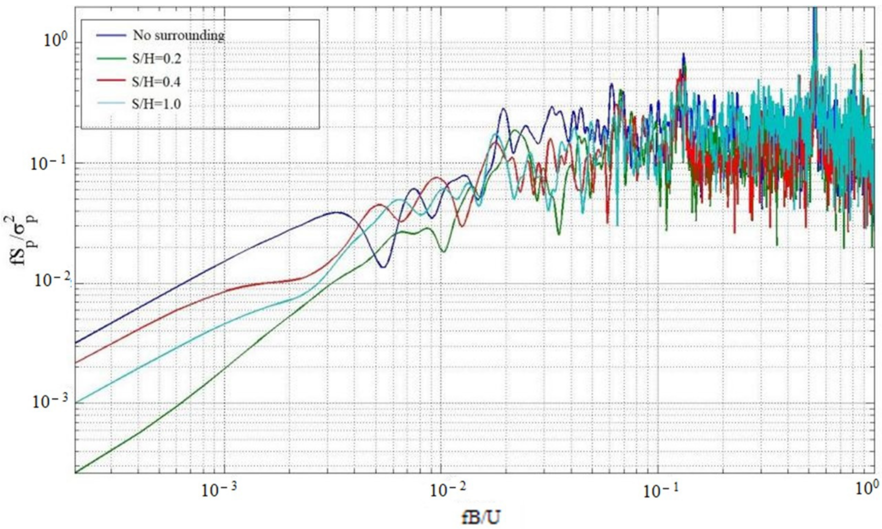


**Figure 19.** Power spectrum analysis of D26.

Figure 20 illustrates that at the measuring point WA1 located at the leeward eave's edge, the spectral peak value of the low-frequency band decreases, and there is a decrease in the spectral peak value of the high-frequency band when compared to the surrounding environment. As the hillside and the building move further apart, the impact of the vortex turbulence generated by the mountain structure diminishes.

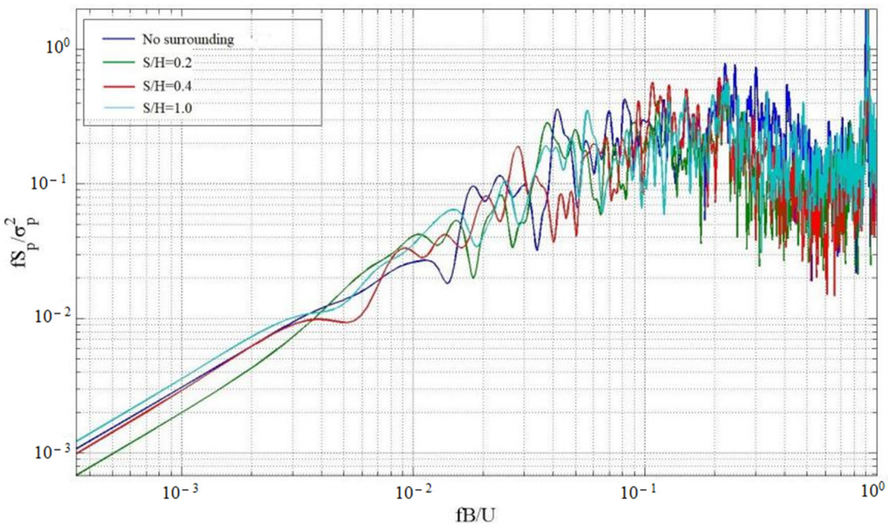


**Figure 20.** Power spectrum analysis of WA1.

Figure 21 illustrates that at a wind direction of 0°, the measuring point WA20 positioned at the center of the windward eave exhibits a significant spectral peak, with a peak value of approximately 0.95 when *S/H* = 0.2 and the low-frequency band reduction frequency is 0.2. When *S/H* = 0.4, as the hillside and the building move further apart, the low-frequency range decreases, and the high-frequency remains insignificant in range. At this time, the influence of incoming turbulence is slightly weakened. When *S/H* = 1.0, the high-frequency energy decreases, and the low-frequency range increases.

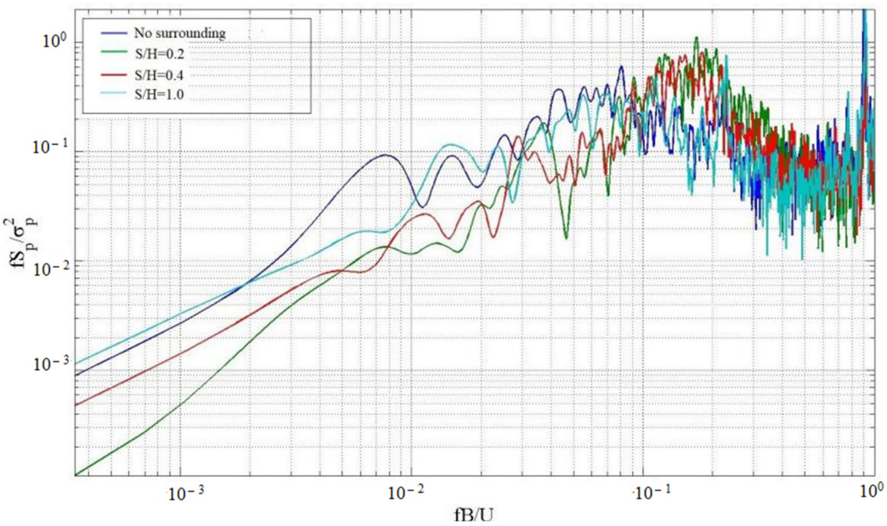


**Figure 21.** Power spectrum analysis of fluctuating pressure on the windward roof.

## 6. Analysis of the Probability Law of Fluctuating Wind Pressure in Low-Rise Buildings

The first-order statistical moment (mathematical expectation) and the second-order statistical moment (variance) are the most commonly used feature parameters to describe the probability density function characteristics of Gaussian signals. However, due to the complexity of non-Gaussian features, multiple moments, such as third-order skewness and fourth-order statistical kurtosis, need to be used to describe the characteristics of the probability density function [28,29].

The skewness of third-order statistics is used to describe the degree to which the probability distribution of wind pressure stochastic processes deviates from the Gaussian distribution. In contrast, the kurtosis of fourth-order statistics is used to describe the degree to which the probability distribution of wind pressure stochastic processes is sharp. The calculation formulas are as follows:

$$C_{Sk} = \sum_{i=1}^{N} [C_{Pi}(t) - C_{Pi,mean})/C_{Pi,rms}]^3/N \tag{9}$$

$$C_{Ku} = \sum_{i=1}^{N} \left[(C_{Pi}(t) - C_{Pi,mean})/C_{Pi,rms}\right]^4/N \tag{10}$$

In the formula, the skewness coefficient and the kurtosis coefficient are shown.

The powerful means to distinguish between non-Gaussian characteristics and Gaussian characteristics are skewness coefficients and kurtosis coefficients(Figure 22). When the distribution is Gaussian, $C_{Sk}$ = 0, $C_{Ku}$ = 3. When testing the degree of deviation of the probability distribution curve, the skewness coefficient is used. When the skewness coefficient $C_{Sk}$ > 0, the Gaussian distribution is biased towards the left relative to the probability distribution, with the maximum estimate larger and the minimum estimate smaller. When the skewness coefficient $C_{Sk}$ < 0, the opposite is true. When testing the flatness of the probability distribution curve, the kurtosis coefficient should be used. When the kurtosis coefficient $C_{Ku}$ > 3, the normal distribution curve is flatter than the probability distribution curve. When using the peak factor method to estimate the extreme values, the values are relatively small. When the kurtosis coefficient $C_{Ku}$ < 3, the situation is the opposite [30]. Kumar [31] set the criteria for judging low-rise houses as greater than 0.5 and kurtosis greater than 3.5 as the boundary between Gaussian and non-Gaussian distribution.

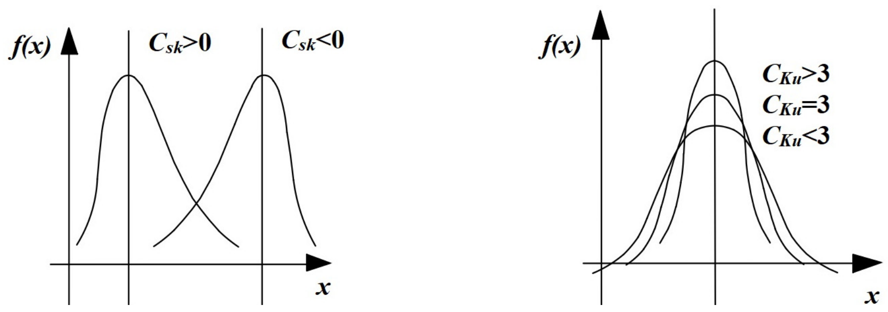


**Figure 22.** Schematic diagram of non-Gaussian characteristic description parameters.

The probability density histograms of representative measurement points are compared, as shown in Figure 23.

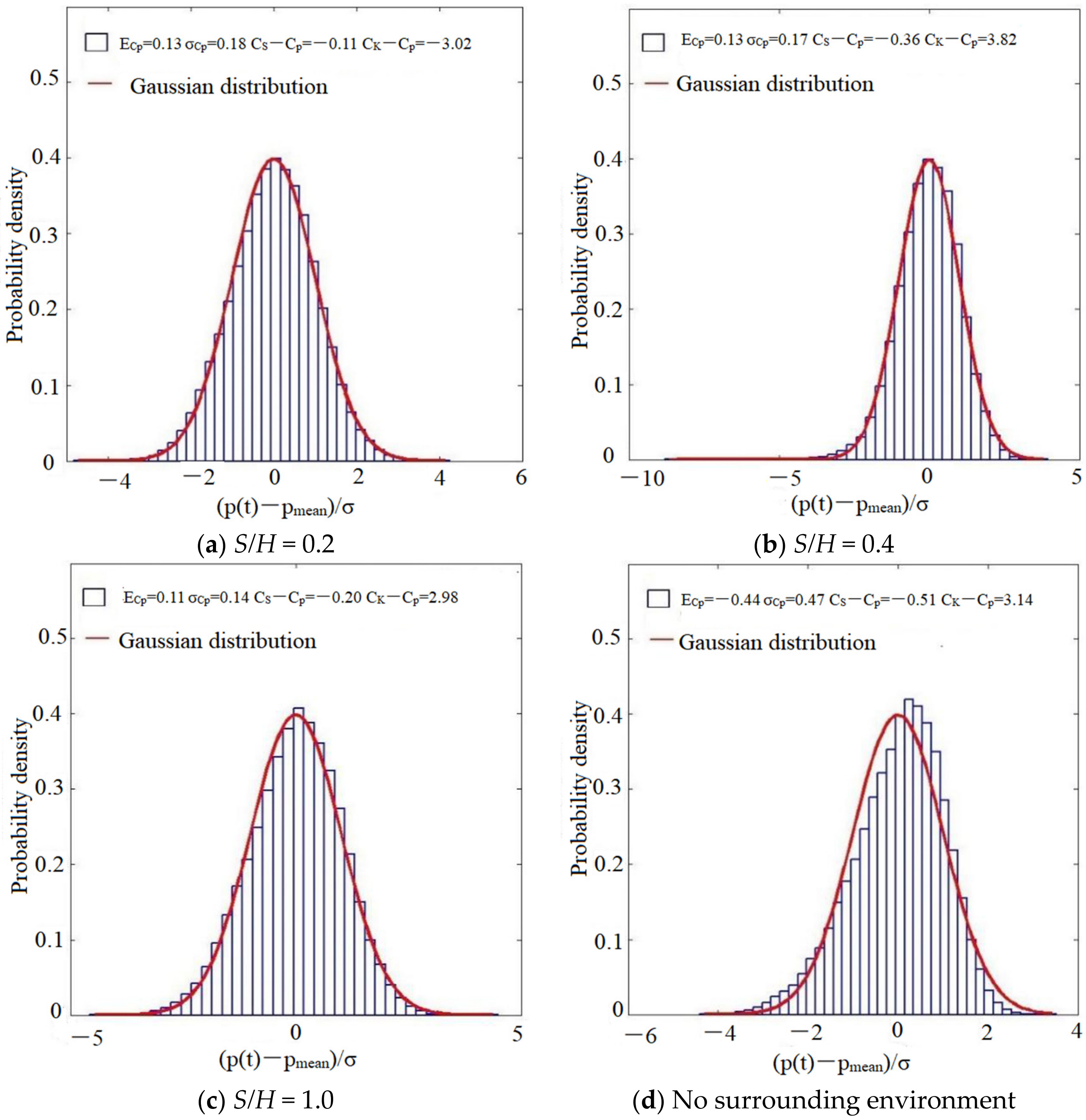


**Figure 23.** A histogram depicting the probability density distribution at D5.

When *S/H* = 0.2, the wind pressure coefficient at the middle of the windward side at 0° exhibits a mean value of 0.13, a root mean square value of 0.18, a skewness of −0.11, and a kurtosis of 3.02. Additionally, the wind pressure probability distribution demonstrates Gaussian characteristics, as evident from above Figure 23. When the hillside and the building are further apart, with a relative position of *S/H* = 0.4, the wind coefficients remain constant. When *S/H* = 1.0, the distribution of wind pressure demonstrates Gaussian characteristics. Without external factors, the parameters exhibit growth, and the wind pressure distribution follows a Gaussian pattern.

As shown in Figure 24, the wind coefficient exhibits Gaussian characteristics in the middle of the left side at a 0° wind direction when *S/H* = 0.2. At *S/H* = 0.4, the probability distribution belongs to Gaussian characteristics. At *S/H* = 1.0, the average and RMS values of the wind pressure coefficient decrease, and the distribution exhibits Gaussian characteristics. Without external factors, it is a non-Gaussian probability distribution of wind pressure.

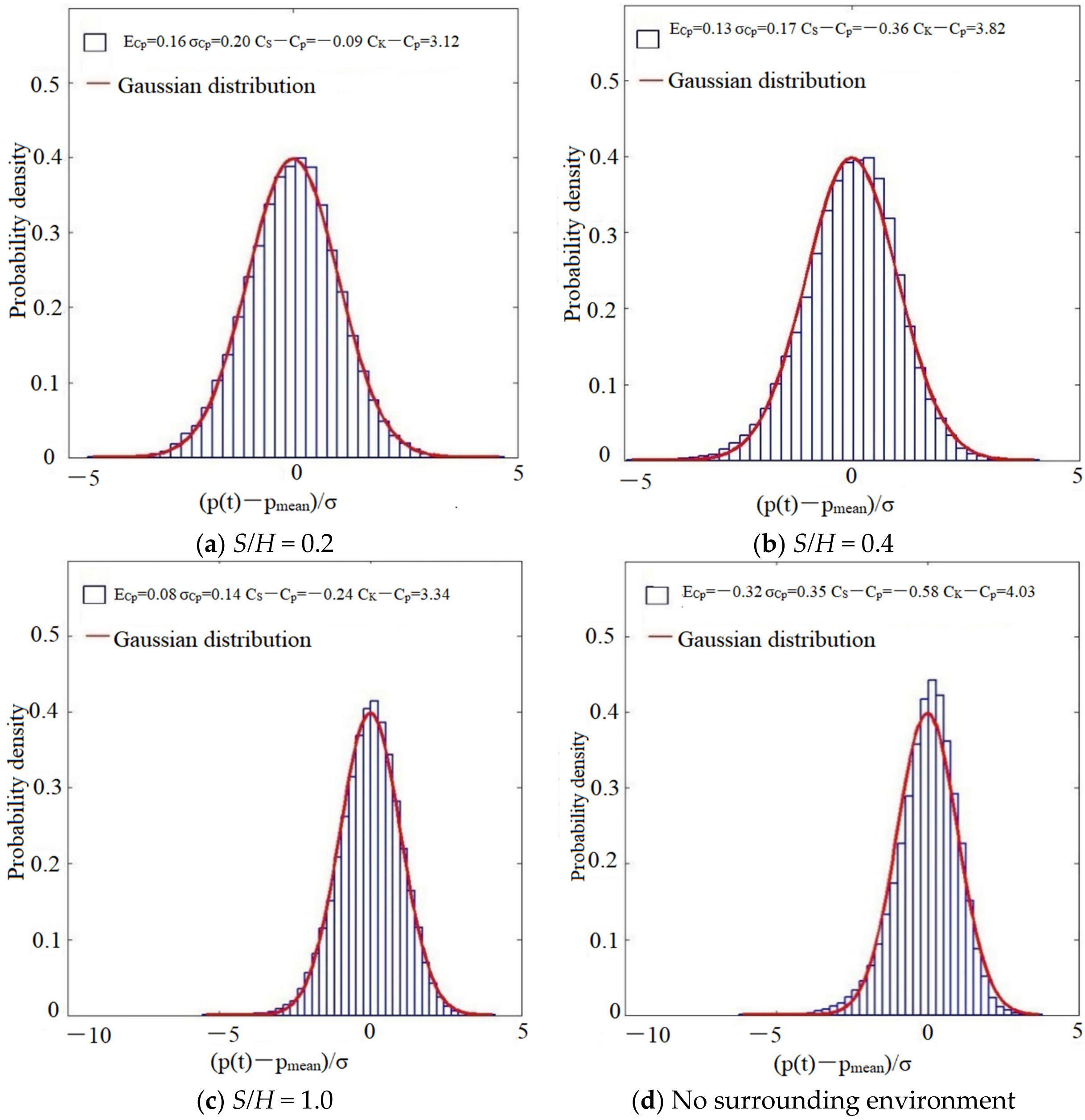


**Figure 24.** A histogram depicting the probability density distribution at D12.

As shown in Figure 25, when *S/H* = 0.2, the wind pressure obeys a Gaussian distribution. At *S/H* = 0.4, the probability wind pressure distribution exhibits Gaussian characteristics. At *S/H* = 1.0, the wind pressure distribution exhibits Gaussian characteristics. Without external factors, it is a non-Gaussian probability distribution of wind pressure.

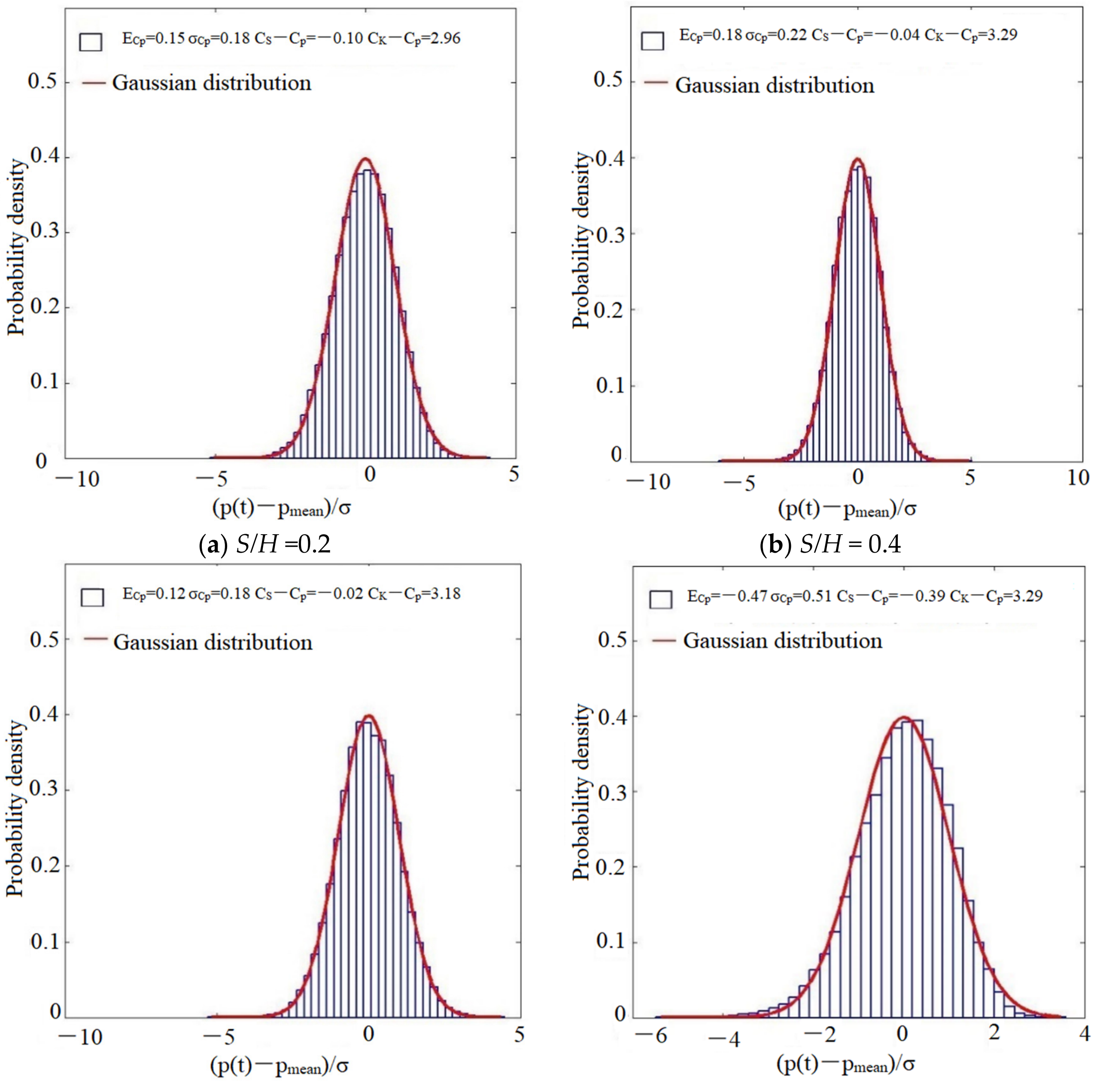


(**a**) *S/H* =0.2 (**b**) *S/H* = 0.4 (**c**) *S/H* = 1.0 (**d**) No surrounding environment

**Figure 25.** A histogram depicting the probability density distribution at D19.

As shown in Figure 26, the wind coefficient exhibits Gaussian characteristics in the middle of the right side at 0° wind direction. When *S/H* = 0.2, 0.4, the distribution exhibits Gaussian characteristics. At *S/H* = 1.0, the probability distribution exhibits non-Gaussian traits. Without external factors, the mean wind pressure coefficient is a non-Gaussian probability distribution.

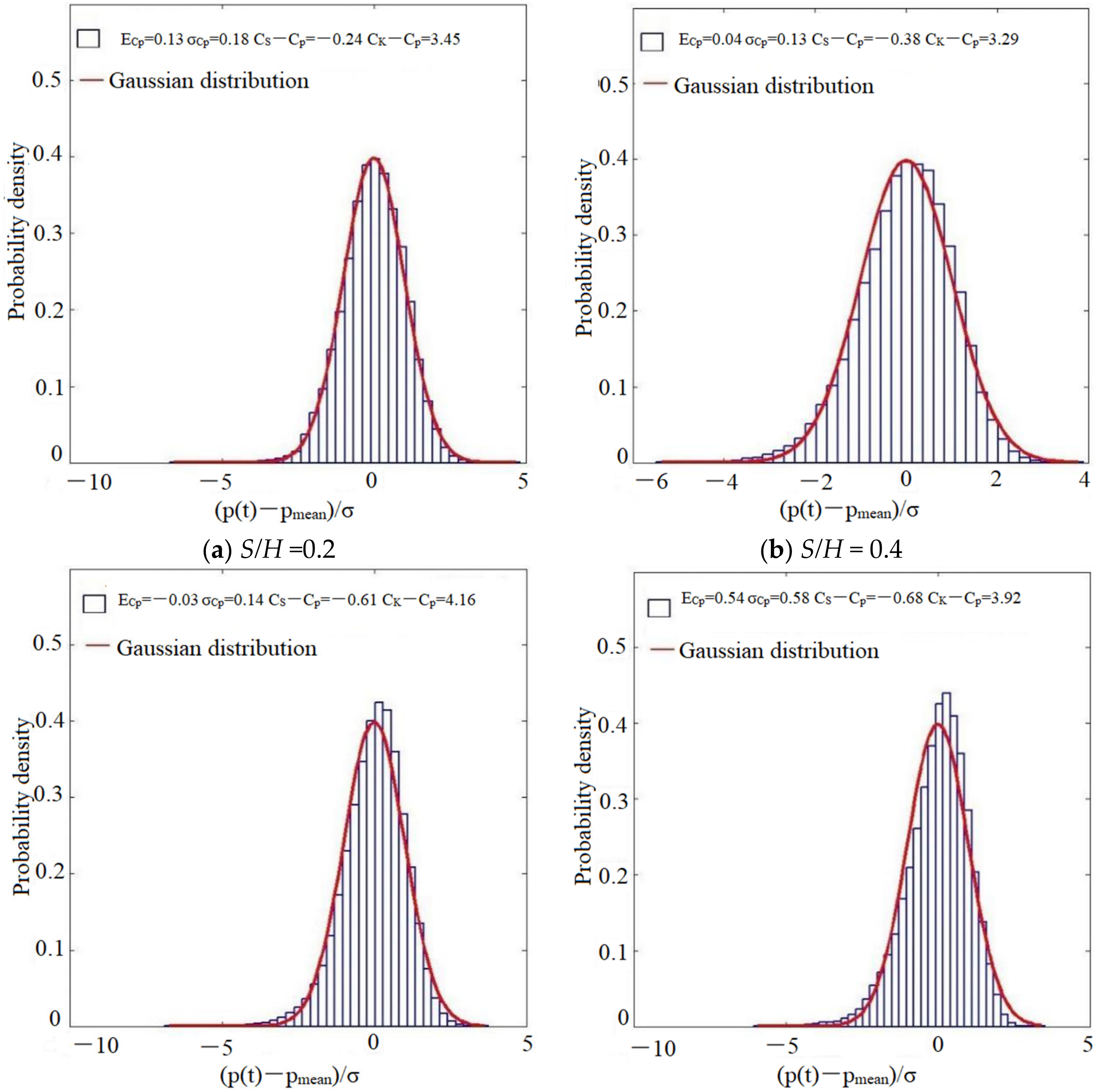

(**a**) *S*/*H* =0.2


(**b**) *S*/*H* = 0.4


(**c**) *S*/*H* = 1.0


(**d**) No surrounding environment

**Figure 26.** A histogram depicting the probability density distribution at D26.

As shown in Figure 27, in the middle of the leeward eave with a wind direction of 0° when *S*/*H* = 0.2, the probability distribution exhibits Gaussian traits. When *S*/*H* = 0.4, the distribution exhibits Gaussian characteristics. At *S*/*H* = 1.0, the average and RMS values of the wind pressure coefficient decrease, and the distribution exhibits Gaussian characteristics. Without external factors, the mean wind pressure coefficient is a non-Gaussian probability distribution.

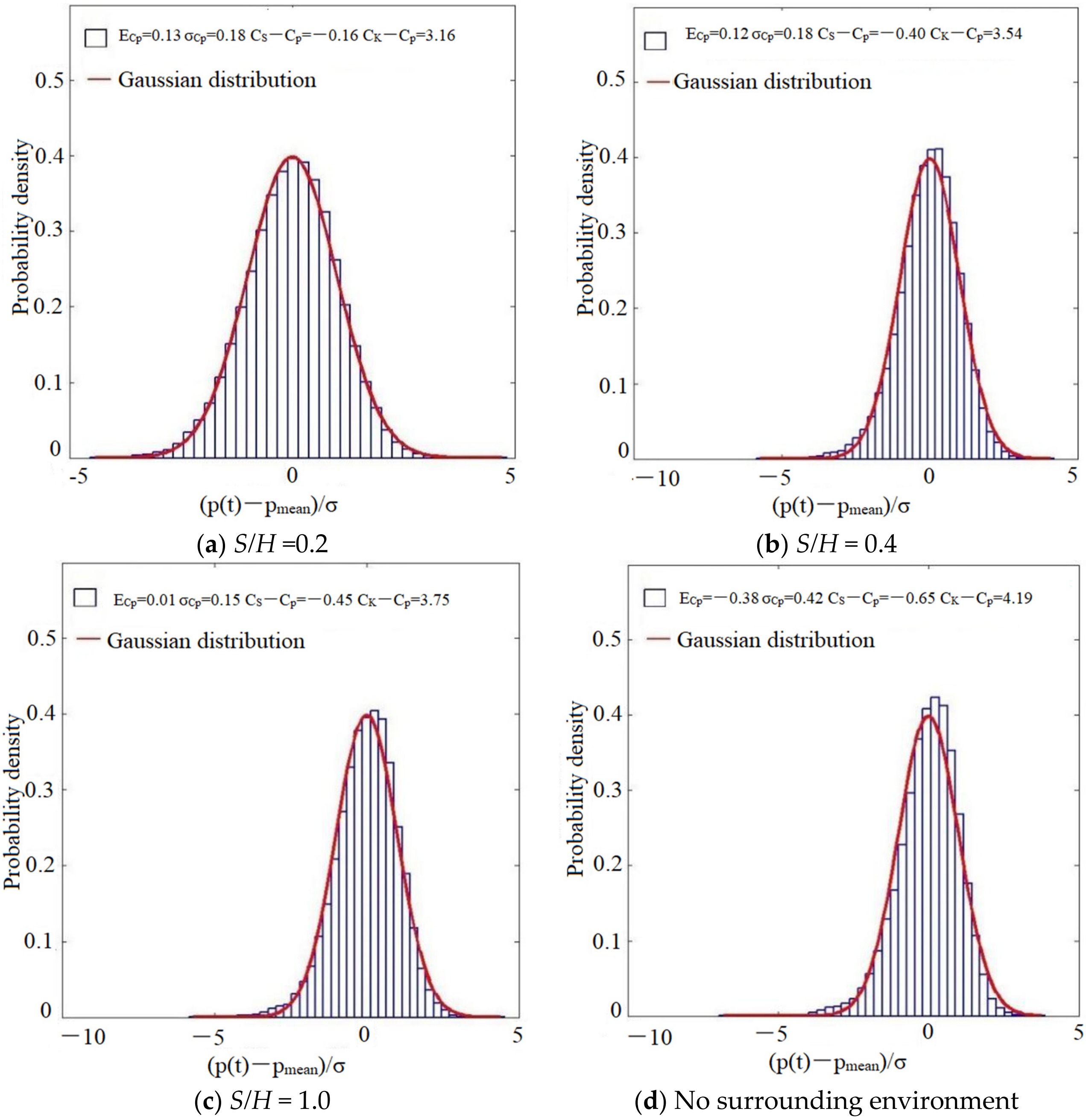


**Figure 27.** A histogram depicting the probability density distribution of wind pressure at WA7.

As shown in Figure 28, the probability distribution in the center of the windward eave with a wind direction of 0° has non-Gaussian characteristics. At *S*/*H* = 0.4, the probability distribution exhibits non-Gaussian characteristics. At *S*/*H* = 1.0, the wind pressure distribution exhibits Gaussian characteristics. Without external factors, the wind pressure coefficient belongs to a non-Gaussian probability distribution.

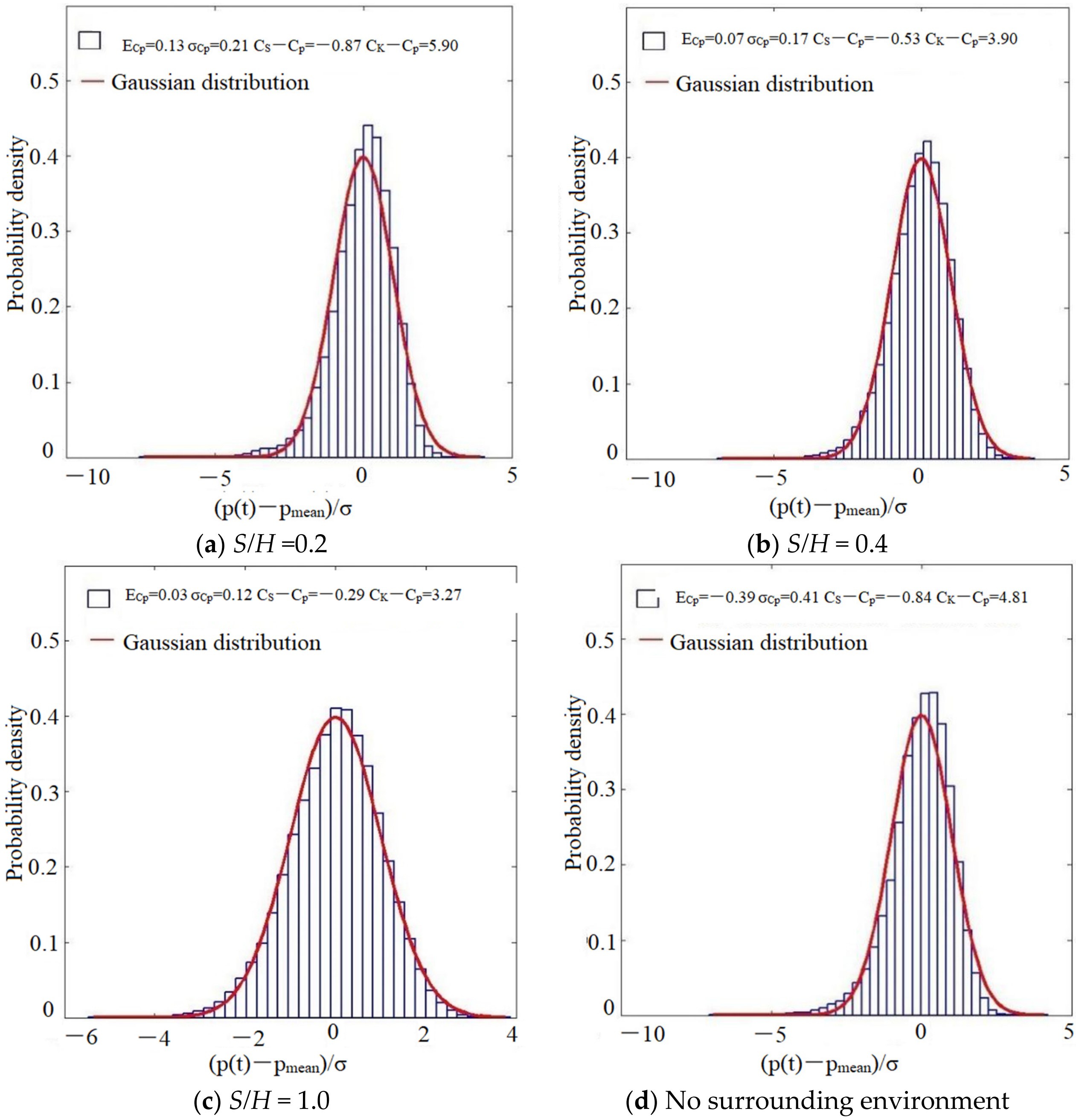


**Figure 28.** A histogram depicting the probability density distribution at WA20.

## 7. Analysis of Flow Field around Low-Rise Buildings Based on Numerical Simulation

### *7.1. Modeling and Solving Process*

#### 7.1.1. Determine the Calculation Basin

When using CFD technology to simulate the flow around a bluff body, the first task is to establish the calculation model. Because the building is located in the atmospheric boundary layer with a completely open-flow wind field, a limited three-dimensional calculation region is used for numerical simulation. It is necessary to ensure that the computational domain is large enough to make enough distance between the boundary and the model and to consider that the number of grids needs to be increased. In the numerical wind tunnel, in general, the requirements for the blockage degree can be expressed as

$$\frac{\text{Maximum windward area of building}}{\text{Cross}-\text{sectional area of watershed}} \times 100\% \; < \; 3\% \tag{11}$$

When CFD is used for numerical simulation, in order to ensure that the computational domain is large enough to keep a certain distance between the model and the boundary, and at the same time, to prevent the problem of a large number of grids and a large amount of calculation caused by too large a computational domain, it is necessary to reasonably set a limited three-dimensional computational domain.

In addition to considering the degree of blockage, it is also necessary to consider whether the setting of the computational domain makes the flow field fully developed. Shi Linglin [32] systematically studied the setting of the computational domain in numerical simulations and summarized the method and standard for selecting the size of the computational domain in view of the influence of hills on low-rise houses in hilly terrain. In order to facilitate the analysis and research, the model is simplified appropriately according to the focus of this paper. In this paper, the influence of the downstream hillside on the wind field around the upstream low-rise houses is studied, and a simplified model is shown in Figure 29.

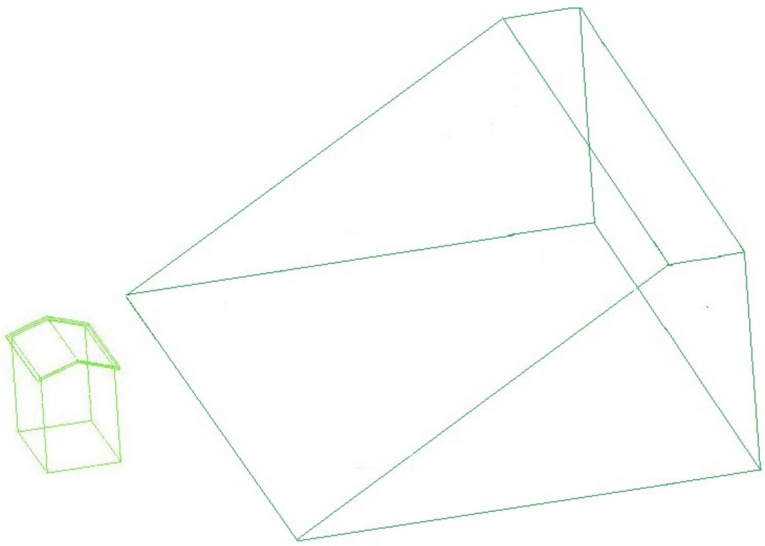

**Figure 29.** Simplified perspective view of the model.

A model of the geometry and its region of spatial influence, i.e., the computational region, is established. In numerical simulation, the numerical wind tunnel should be established first. The size of the numerical wind tunnel is closely related to the calculation accuracy. If it is too small, it will affect the wind pressure distribution on the surface of the building. If it is too large, it will increase the number of grids.

In addition, the blocking rate should meet the requirements to ensure that the flow field can be fully developed; this is also a matter of attention when calculating the fluid domain. The study shows that the height of the computational domain depends mainly on the shape and size of the windward side of the target object. For the computational domain of low-rise buildings, the distance from the entrance to the windward side of the building should be 4 H~5 H, the distance from the side of the building to the boundary of their respective watersheds should be more than 4 H, and the distance between the top of the building and the top of the flow field should be more than 5 H. In order to fully develop the turbulence, the leeward side of the building should be 10 H to 15 H away from the outlet. The maximum blocking rate of the numerical simulation model in this paper (as shown in Figure 30) is 1.8% < 3%, which meets the requirements.

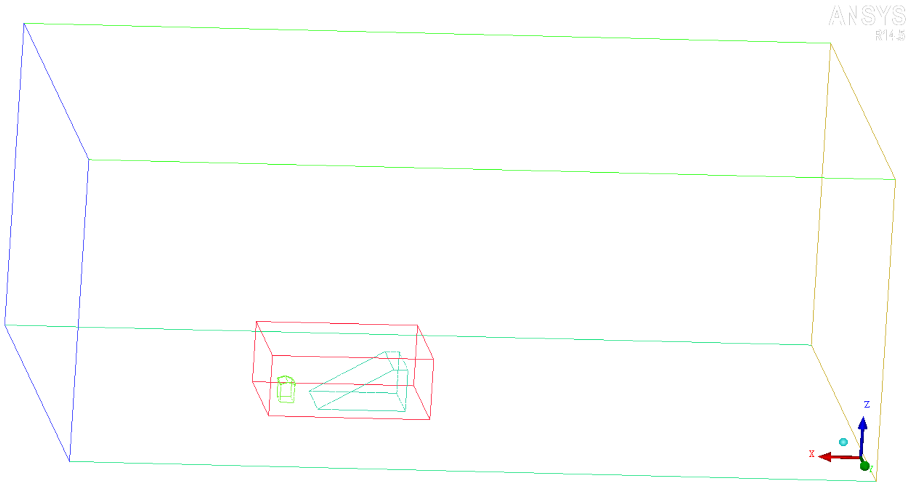


**Figure 30.** Fluid calculation domain.

#### 7.1.2. Grid Division

In this paper, the hybrid meshing method is used to mesh the model. Different regions are meshed in different ways. In the inner region near the building structure, unstructured tetrahedral mesh can be refined, which is convenient for capturing the changing characteristics of physical phenomena such as the shear layer and vortex motion. In the outer region far from the building, high-quality structured hexahedral mesh is usually partitioned in the flow field. In the boundary layer close to the building wall, a minimum grid size of 0.04 mm is set. After calculation, the dimensionless grid size y + near the building wall is between (1 and 3), which meets the requirements of large eddy simulation except for a few points. In addition, the aspect ratios of the grid cells are all above 0.2, and the grid expansion factors of two adjacent cells are not more than 1.2. The mesh quality should meet the computational requirements of the numerical simulation. Figure 31 shows the division of the fluid computational domain grid (left) and the local grid (right). The number of grids for each model in this chapter is different, ranging from 1 million to 1.5 million.

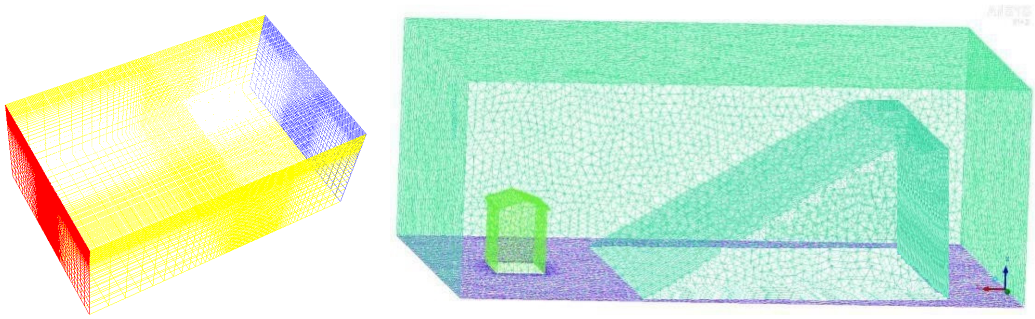

**Figure 31.** Division of fluid computational domain grid (**left**) and local grid (**right**).

#### 7.1.3. Setting of Boundary Conditions

(1) Inlet boundary conditions

In order to effectively compare the results with the wind tunnel test results, it is necessary to simulate the same wind profile as the wind tunnel test to simulate the B landform and to take the reference point at a height of 0.25 m corresponding to the undisturbed 10 m upstream of the building.

The expression for the wind profile is

$$v_z = v_{10}\left(\frac{z}{10}\right)^{\alpha} \tag{12}$$

where $v_{10}$ is a wind speed of 8 m/s at a height of 10 m of the wind profile during the wind tunnel test.

Turbulence intensity: In this paper, the turbulence intensity of the Class B wind field is simulated by referring to the provisions of Japanese specifications for the turbulence intensity of Class II roughness. The expression of turbulence intensity is as follows:

$$\begin{cases} I_u = 0.23\ Z < Z_0 \\ I_u = 0.1(Z/Z_G)^{-\alpha-0.05}\ Z > Z_0 \end{cases} \quad (13)$$

The average wind speed profile and turbulence intensity profile of the incoming flow of the wind field are obtained from the wind speed time history curves of 10 points monitored at equal intervals at different heights near the same plane, as shown in Figure 32. It can be seen from the figure that the theoretical value is in good agreement with the average wind speed profile, the turbulence intensity decreases gradually with the increase in height, and the value is between the Chinese specification and the Japanese specification.

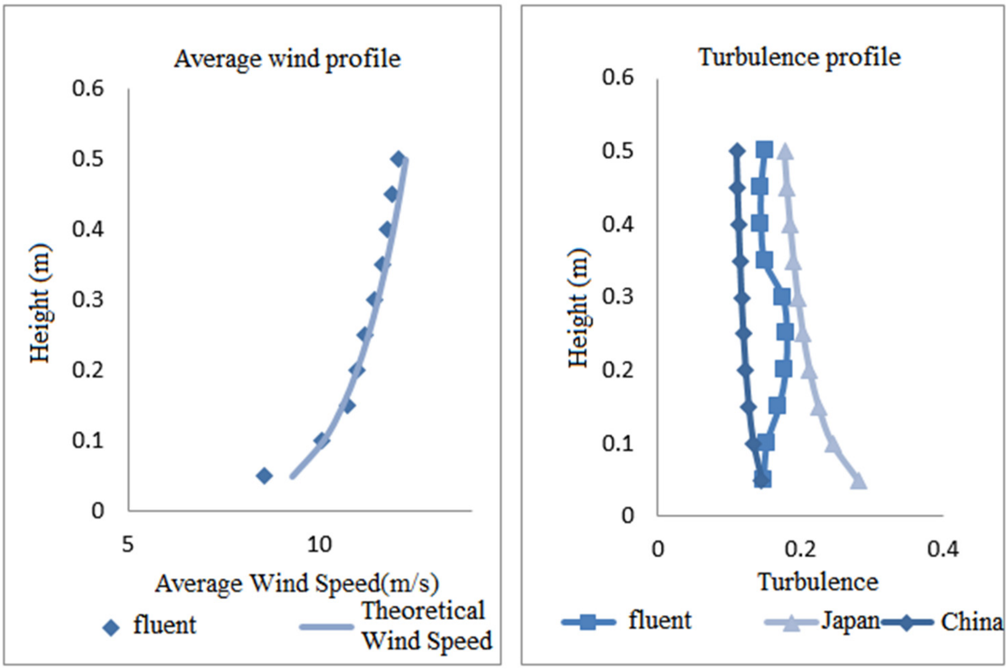


**Figure 32.** Profile of mean wind and turbulence at the entrance of the calculation domain.

The wind speed time histories at the 10 m height of the LES monitoring point were analyzed (Figure 33), and the LES wind speed spectra were plotted (Figure 34). It can be seen from Figure 34 that the wind speed spectrum of the large eddy simulation is more consistent with the Von Karman spectrum, and the turbulence fluctuation characteristics at the inlet turbulence are more realistic when they are used to simulate the fluctuation characteristics of the atmospheric boundary layer.

(2) Outlet boundary condition: The free outflow boundary is selected, and the velocity gradient is 0 along the normal direction of the outlet boundary;
(3) On the top and both sides of the basin: Symmetry boundary conditions are selected, which are equivalent to the free slip wall in viscous flow;
(4) Building surface and ground: A no-slip wall condition is selected.

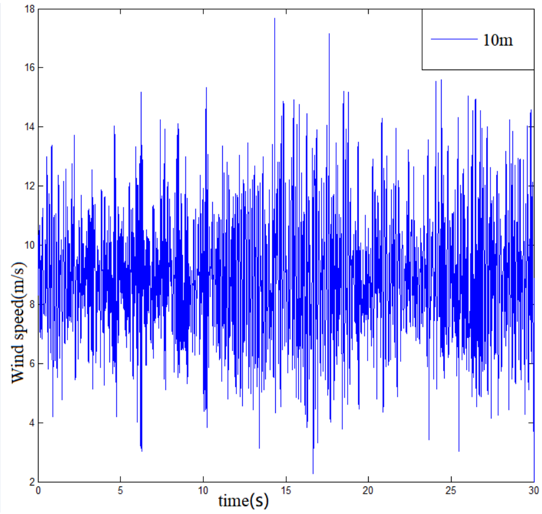


**Figure 33.** Wind speed time history.

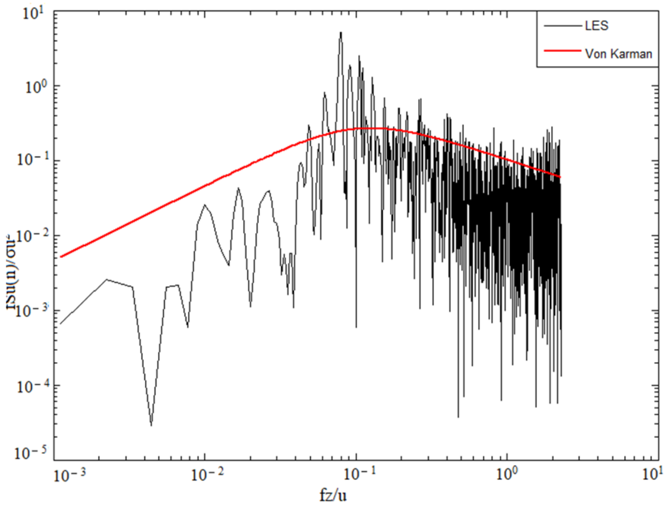


**Figure 34.** Power spectrum of wind speed.

#### 7.1.4. Turbulence Model Selection and Wall Treatment Method

Incompressible air with constant density is selected as the fluid model, the flow Reynolds number of the numerical simulation is set to the order of magnitude, and the material parameters are set to the default.

Because the standard model of the k-ε two-equation turbulence model has high accuracy and stability, it is suitable for high Reynolds number turbulence, so the standard model is selected for calculation. Because the standard model is valid only for the fully developed high Reynolds number turbulent flow, in the flow limited by the wall, the gradient of the flow field variables near the wall is large. In order to solve the influence of the wall viscosity, the standard wall function method is used in this paper.

#### 7.1.5. Solution Method and Convergence Control

(1) Selection of solution method

To create the initial flow field for the following transient calculation, the numerical simulation first uses the Reynolds Average Method, which has fast convergence and uses less calculation time to carry out the steady-state calculation. During the steady-state calculation, the turbulent model, which is stable and accurate, is selected to simulate the turbulent flow. The method of enhanced wall treatment is used to supplement it. The SIMPLEC method is used to decouple the velocity-pressure equations, and the second-order upwind scheme (Second-Order Upwind) is used to discretize the equations. The incompressible air with default material parameters is selected as the fluid material in the flow field calculation domain. When the steady-state calculation is converged, the GUI command is used to make the steady-state flow field have the characteristics of a transient flow field, and the large eddy simulation (LES) method is used for transient calculation.

The classical Smagorinsky–Lilly model is used to calculate the LES, and the SIMPLEC method based on the decoupling idea is used to solve the discrete equations. The standard scheme is used to discretize the pressure term, the central difference scheme (Bounded Central Differencing) is used to discretize the momentum equation, and the second-order implicit scheme (Second-Order Implicit) is used to discretize the transient equation.

(2) Convergence control

In general, the convergence criterion is reduced to the residual by three orders of magnitude during the numerical calculation process. For steady-state simulation calculation, the convergence standard in this paper is set to reduce the residuals of each term to less than 10-5; for transient modal fitting (this paper refers to large vortex modal fitting), the convergence criteria in this paper are set to four orders of quantity.

(3) Setting of time step

The most significant difference between transient simulation and steady-state simulation is the need to define the analysis type as transient and set the time and step of the simulation calculation. In the transient simulation, the time step should be reasonably selected. When the time step is large, the data points saved in the transient calculation cannot reflect the real flow field state, and the small time step can not only speed up the convergence of the calculation, but also reflect the turbulence fluctuation characteristics more truly. However, too small a step will increase the calculation time. In order to obtain stable calculation values and ensure that the turbulent fluctuation characteristics can be fully reflected, the following estimation method is proposed to set the time. The result is shown in Figure 35. First of all, in order to solve the numerical value stably in the large eddy simulation, the Courant–Friedrichs–Lewy number, i.e., NCFL, should satisfy the following relation:

$$N_{CFL} = max\left(\frac{\Delta t|u|}{\Delta x}, \frac{\Delta t|v|}{\Delta y}, \frac{\Delta t|w|}{\Delta z}\right) < 1 \quad (14)$$

where $\Delta x$, $\Delta y$, and $\Delta z$ are the scale components of the grid in the $x$, $y$, and $z$ directions, respectively. In the large eddy simulation, the time step is 0.005 s, and each time step is iterated 20 times. The flow field reaches a stable state after about 5 s, and then 30 s of data are continuously collected for analysis.

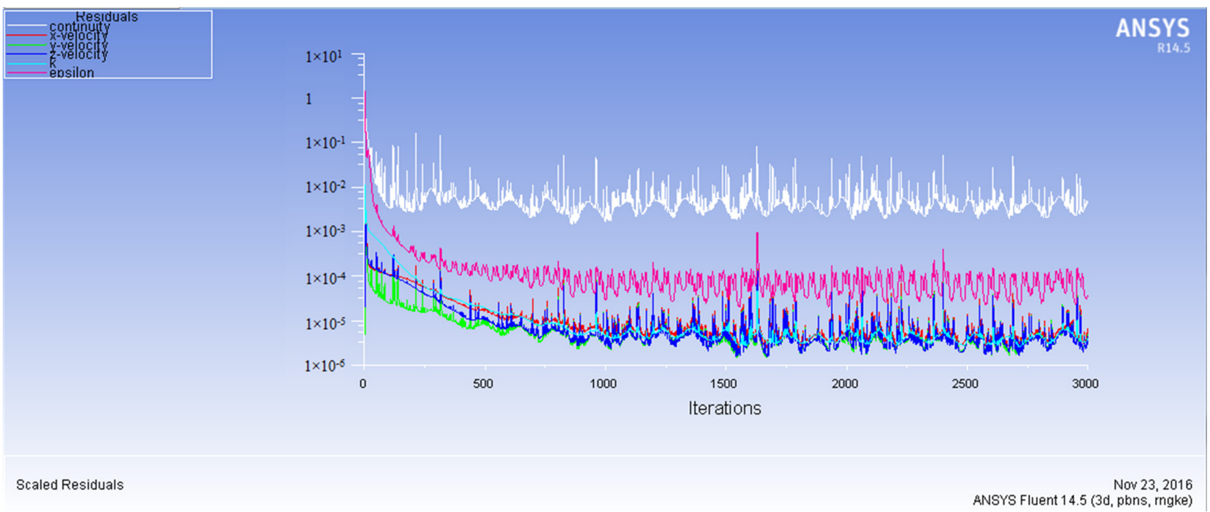


**Figure 35.** Residual convergence curve of steady-state calculation.

### *7.2. Comparison between Wind Tunnel Test and Numerical Simulation*

In order to verify the accuracy of the numerical simulation, the numerical simulation data are compared with the wind tunnel data. As there are many working conditions, three common working conditions are selected for comparative analysis. Figure 36 shows the working condition of $\beta$ = 60°, *S/H* = 1.0, and *Hm/H* = 2.0. Figure 36 shows that $\beta$ = 60°, *S/H* = 0.4, and *Hm/H* = 2.0.

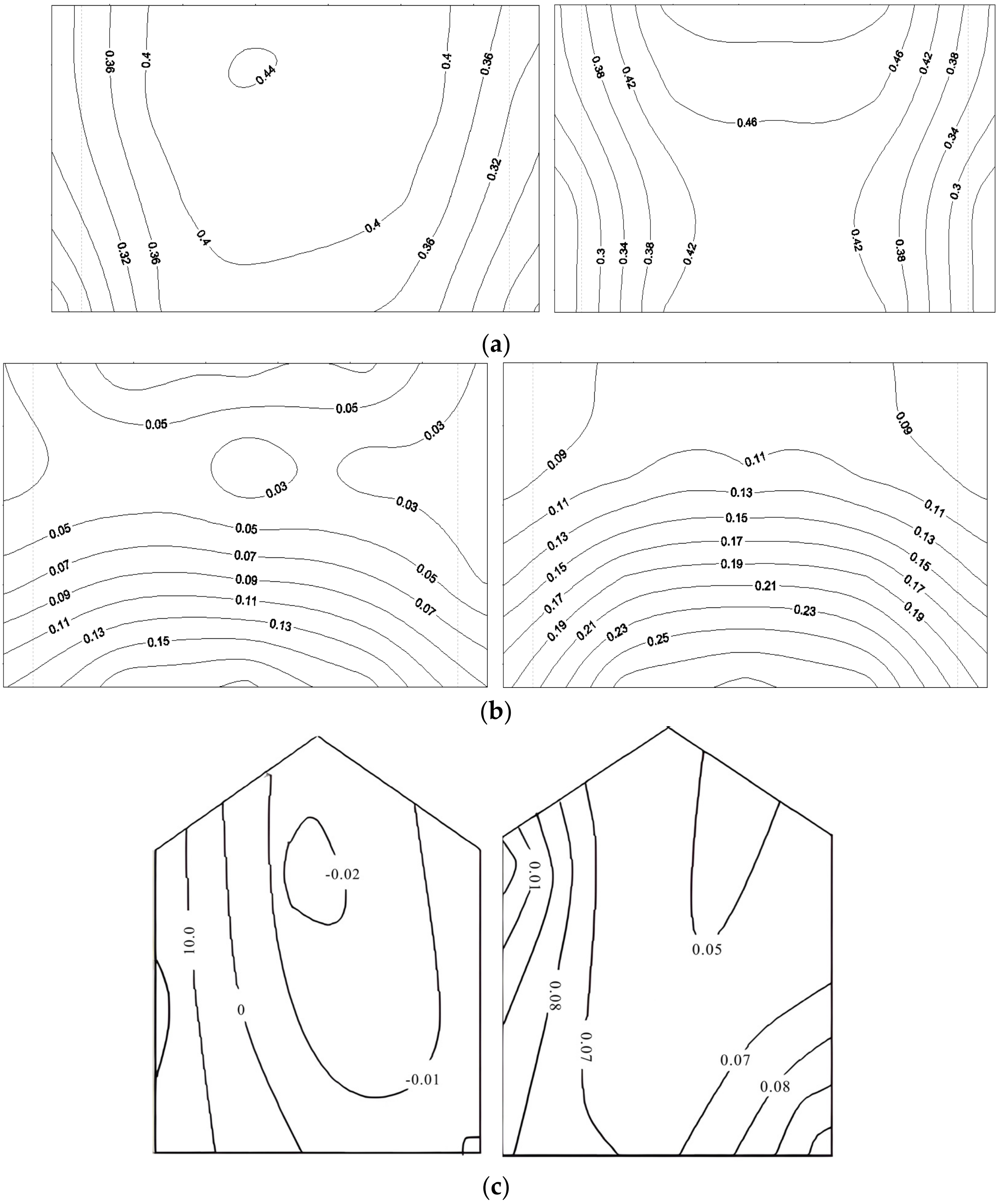


**Figure 36.** *Cont.*

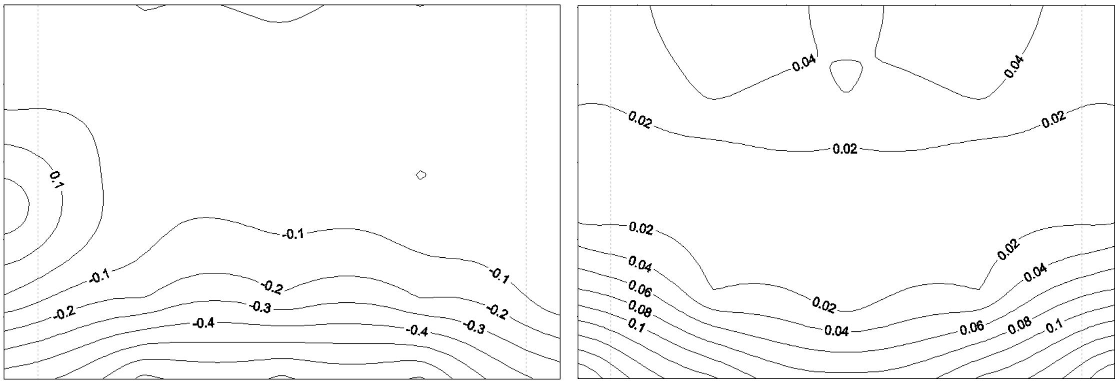


(**d**)

**Figure 36.** Distribution of average wind pressure coefficient on each building surface at $\beta$ = 60°, *S/H* = 1.0, and *Hm/H* = 2.0. (**a**) Windward side (wind tunnel test results (left) and numerical simulation results (right)); (**b**) leeward side (wind tunnel test results (left) and numerical simulation results (right)); (**c**) side (wind tunnel test results (left) and numerical simulation results (right)); (**d**) roof (wind tunnel test results (left) and numerical simulation results (right)).

In Figure 37, comparing the isosceles of the average wind pressure coefficients on the surface of low buildings and low buildings with mountain bodies, the results show that:

(1) For the wind pressure distribution of the back wind surface of low-rise buildings, the numerical simulation results are different from the corresponding wind tunnel test results. This is mainly due to the influence of the tail flow on the wind pressure distribution on the back wind surface, and at the same time, because the geometric scale model is used in the test, it is impossible to fully reflect the response of the structure under the detailed wind load, so the average wind pressure coefficient is different from that obtained by the wind tunnel experiment and the numerical simulation.

(2) For the wind pressure distribution on the side of the building, there is a certain trend of the average wind pressure coefficient due to the disturbance of the hillside and the generation of a vortex.

(3) For the roof, the numerical simulation results are quite different from the corresponding wind tunnel test results, both with the distribution law and with the numerical value. The main manifestation is that the numerical simulation results do not show the effect of the separation of air flow at the roof ridge on the local wind pressure coefficient of the roof. For example, when there is no peripheral working condition, the air flow separates at the roof ridge of the windward roof, and the local wind pressure increases rapidly, forming a high negative pressure area. The wind tunnel test results describe this phenomenon well, but the numerical simulation results do not show this phenomenon. The main reason is that the turbulent flow predicted by the standard turbulent model using the separation zone of the top of the passive body is higher than that predicted by the high ground, and the turbulent kinetic energy generation term of the top of the passive body impacting the wind surface is higher than that estimated by the standard turbulent model, which leads to the inaccurate pressure distribution of the top wall of the building. Further improvement may be needed in specific applications.

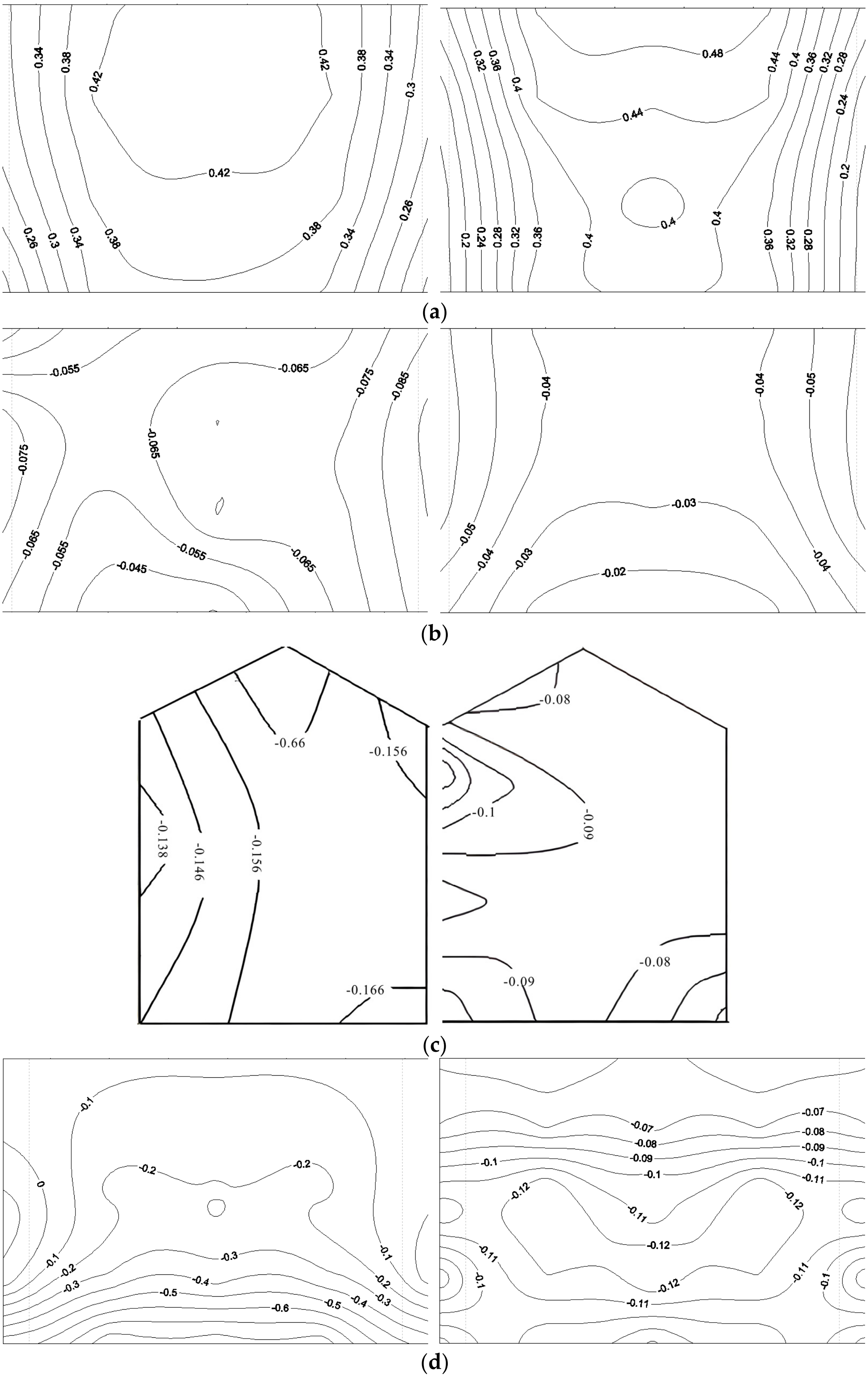


**Figure 37.** Contour map of mean wind pressure coefficient on each building surface at $\beta$ = 60°, $S/H$ = 0.4, and $Hm/H$ = 2.0. (**a**) Wind surface (wind tunnel test results (left) and numerical simulation results (right)); (**b**) leeward side (wind tunnel test results (left) and numerical simulation results (right)); (**c**) side (wind tunnel test results (left) and numerical simulation results (right)); (**d**) roof (wind tunnel test results (left) and numerical simulation results (right)).

*7.3. Numerical Simulation Analysis of Distance Change between House and Hillside*

Next, we discuss the influence of a further increase in the distance between the low-rise building and the back hillside on the wind pressure distribution characteristics of each surface of the building. In this paper, the numerical simulation method is used to calculate the $S/H$ = 2, $S/H$ = 4, and $S/H$ = 10 conditions. The result is shown in Figure 38.

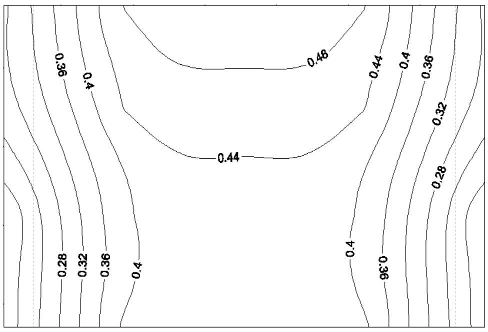


(**a**) $S/H = 2.0$

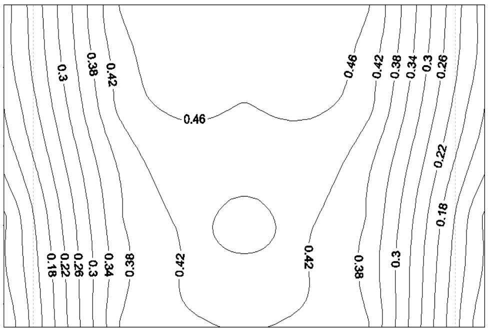


(**b**) $S/H = 4.0$

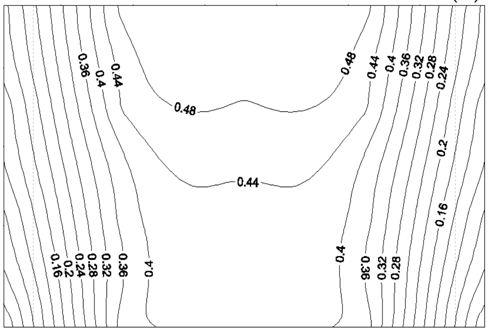


(**c**) $S/H = 10.0$

(1) Windward side

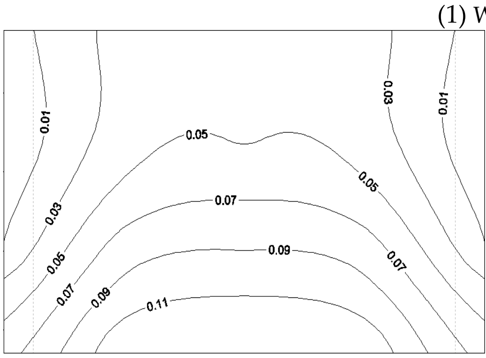


(**d**) $S/H = 2.0$

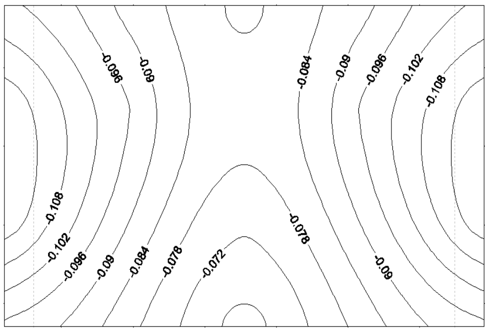


(**e**) $S/H = 4.0$

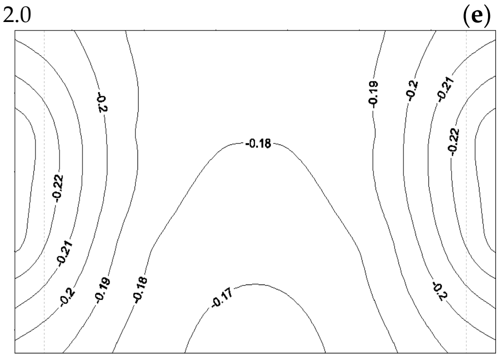


(**f**) $S/H = 10.0$

(2) Leeward side

**Figure 38.** *Cont.*

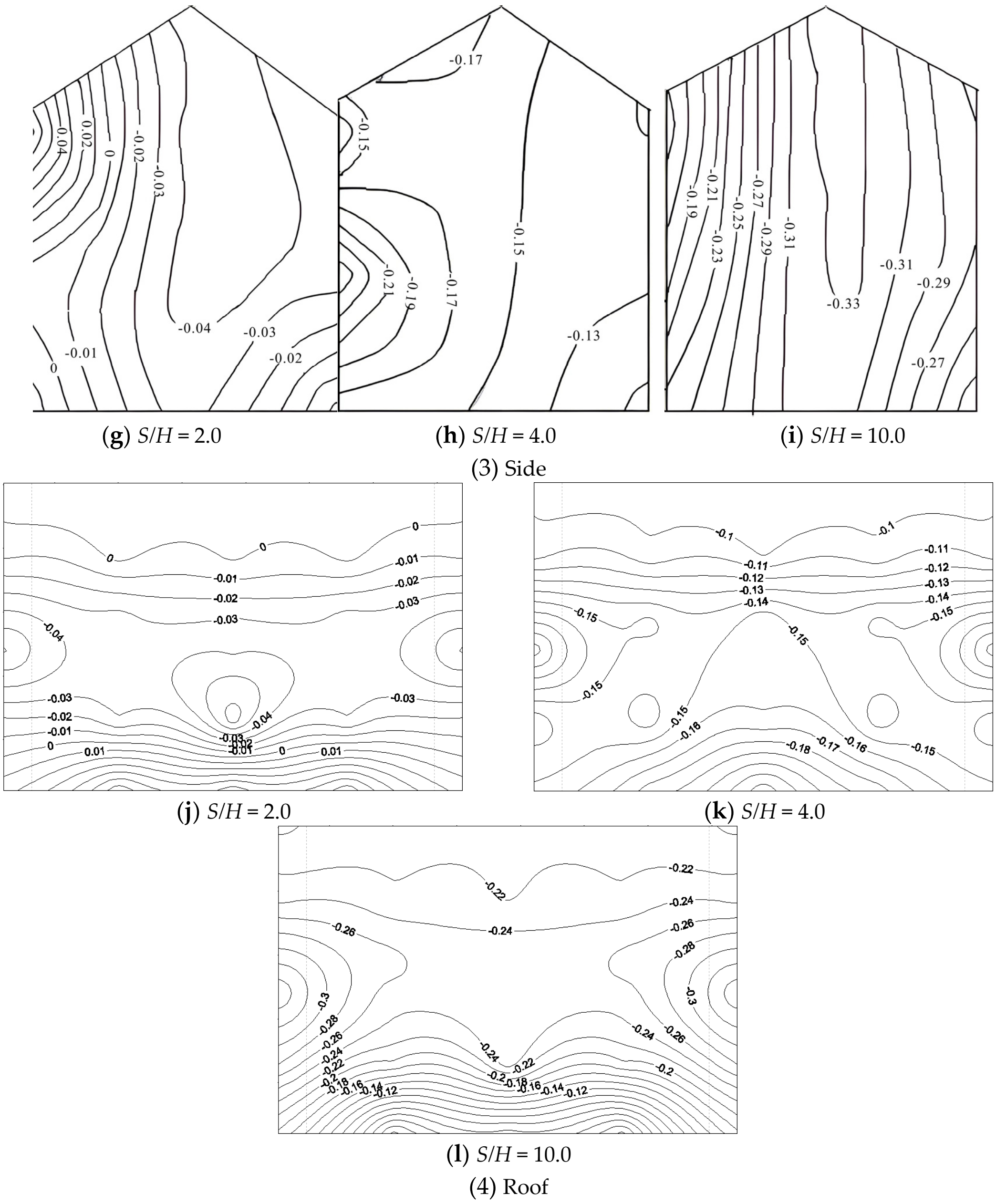


**Figure 38.** Distribution of wind pressure coefficient on the surface of each building changing with the distance from the building to the hillside.

Comparing the results of CFD simulations with wind tunnel tests, it was found that although there are certainly differences between the two, their impact on each side of the house is similar. The existence of a hillside has a more pronounced effect on the gable wall and leeward roof surface. Due to size constraints in the wind tunnel test, where the distance between the hillside and the low-rise houses is relatively small, a bigger distance was chosen when using CFD for simulation.

It can be seen from Figure 38 that when $S/H = 2$, the average wind pressure coefficient distribution of each surface has little change compared with that when $S/H = 1$. Specifically, the wind pressure distribution of the windward wall surface is hardly affected by the rear hillside, and the leeward wall surface and the side surface gradually change from negative pressure to positive pressure with the increase in the hillside slope. The absolute value of the wind pressure coefficient of the roof decreases gradually, which indicates that the influence of the hillside on the wind load of the roof is smaller. Generally speaking, the influence of the rear hillside on the windward wall of the house is not great. For other building surfaces, when the distance between the hillside and the house is within a certain range, with the increase in the distance between the hillside and the house, the influence of the hillside on the wind load on the surface of the house becomes smaller and smaller, and when the distance between the hillside and the house reaches a certain value, the influence can be ignored.

Due to the close correlation between the average wind pressure coefficient on the surface of low-rise buildings and the flow pattern of gas around the buildings, to study the mechanism of wind pressure distribution in low-rise buildings, based on CFD numerical simulation technology, the flow field around low-rise building and mountain was simulated, and the flow pattern of airflow around low-rise buildings and mountains was summarized.

As shown in Figure 39, after adding the mountain, a vortex formed between the mountain and the low-rise building, changing the flow field distribution of the low-rise building, with the influence of the leeward side being particularly significant. As the relative position between the slope and the building increases, the influence of the formed vortex on the surface of low-rise buildings gradually weakens. As the slope of the mountain increases, the vortex formed between the mountain and the building gradually moves downwards. At a 90° wind angle, the wind speed on the roof and leeward side changes significantly compared to 30°, and the suction on the roof and leeward side gradually turns into pressure.

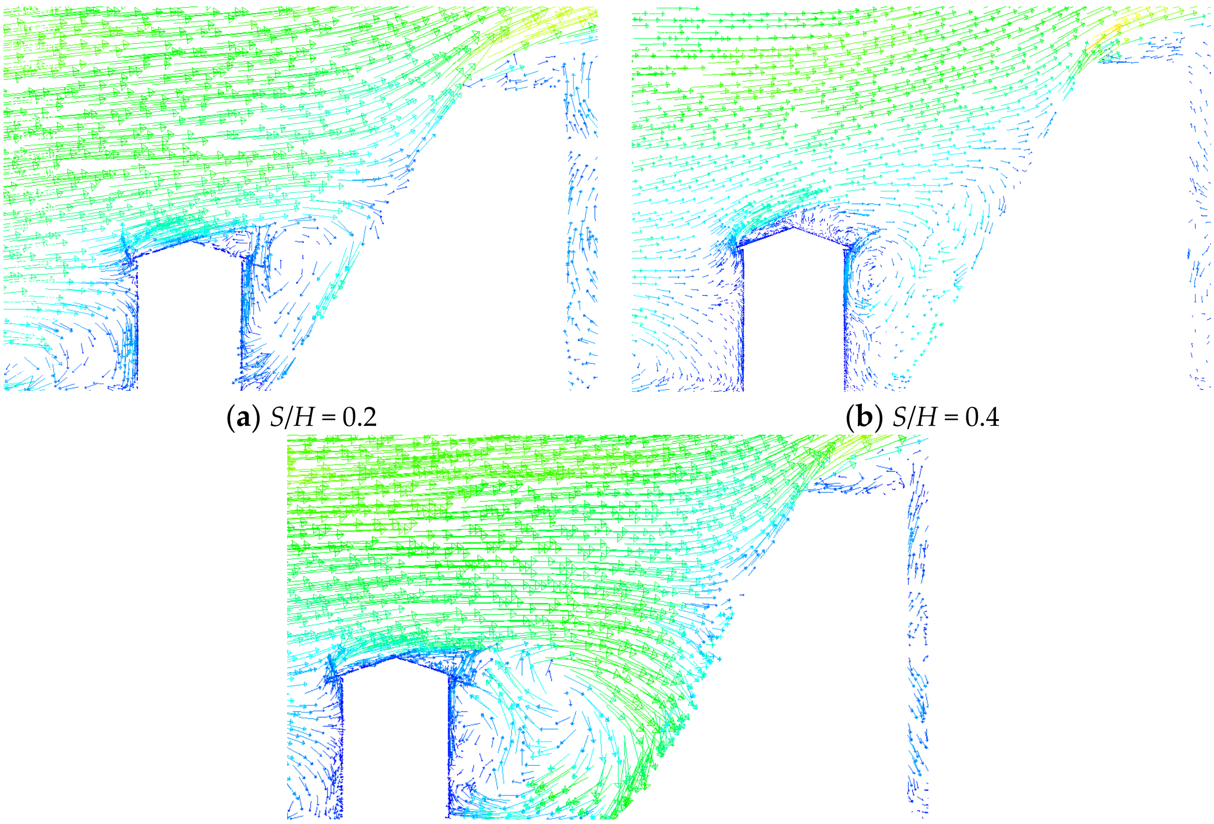

(**a**) $S/H = 0.2$ (**b**) $S/H = 0.4$

(**c**) $S/H = 1.0$

**Figure 39.** Flow field changes with the relative position of the mountain slope and buildings.

## 8. Conclusions

This article comprehensively analyzes and studies the variation law of pulsating wind pressure characteristics of low-rise buildings under mountain terrain with spacing through wind tunnel experiments and summarizes the variation law of probability distribution of pulsating wind pressure when the measurement points change with the relative position between the mountain slope and the building. Here, we summarize the most unfavorable working conditions and locations that may occur, providing a basis for the wind resistance design of low-rise buildings in the future.

1. As the distance between the slope and the mountain increases, the fluctuating wind pressure coefficient continues to increase, and the contour lines of the wind pressure distribution are relatively denser compared to where there is a mountain. The maximum value of the fluctuating wind pressure coefficient is 0.22, which appears at the windward roof. The wind pressure coefficient on the building surface varies in a specific manner as the distance between the hillside and the building grows. The fluctuating coefficient on the windward side decreases first and then increases. The fluctuating coefficient on the left and right sides increases gradually. At infinity, the value decreases when there is no influence from the surrounding environment. The fluctuating coefficient of the roof increases gradually and reaches the maximum when there is no influence from the surrounding environment.
2. Due to the existence of the mountain, the energy of the low-frequency band is weakened, and the energy of the high-frequency band is enhanced. This is mainly due to the suppression of the spatial large-scale vortex structure by the mountain, resulting in the weakening of the turbulence characteristics of the incoming wind and the increase in the small-scale vortex. With the increasing distance between the hillside and the building, the energy in the low-frequency band at the windward eaves decreases, and the energy in the high-frequency band increases gradually.
3. The variation in the probability distribution of wind pressure at the middle measuring points in different regions under 0° wind direction was analyzed, and it was found that with the increase in the relative position between the hillside and the building, the probability distribution has Gaussian characteristics when the leeward side has no periphery under the three working conditions. In the middle of windward and leeward eaves, the distribution characteristics gradually changed from non-Gaussian characteristics to Gaussian characteristics.
4. Due to the presence of the mountain, the airflow forms a vortex between the hillside and the low-rise building, thereby changing the flow field distribution of the low-rise building, especially the wind pressure distribution on the leeward side. As the relative position between the slope and the building increases, the influence of the vortex formed on the surface of low-rise buildings gradually weakens. Overall, the impact of the rear slope on the windward wall of the house is not significant. For other building surfaces, when the distance between the slope and the house is within a determinate range, as the distance between the slope and the house increases, the impact of the slope on the wind load on each surface of the low-rise building becomes smaller. When the distance between the slope and the house reaches a determinate value, the impact of the hillside can be ignored.

**Author Contributions:** Software, M.Z., C.W. and X.W.; formal analysis, M.Z. and M.L.; investigation, C.W. and X.W.; resources, M.Z. and C.W.; data curation, M.L., J.L. and M.Z.; writing—original draft preparation, M.Z., M.L. and C.W.; writing—review and editing, J.L. and X.W. All authors have read and agreed to the published version of the manuscript.

**Funding:** The work described in this paper was supported by the Science Research Project of the Hebei Education Department, grant number BJ2020010, and the National Natural Science Foundation of China, grant numbers 51478179 and 51178180.

**Data Availability Statement:** The data are open-source data; please contact the author if needed.

**Conflicts of Interest:** The authors declare no conflicts of interest.

## References


1. Fan, Y.; Quan, Y.; Gu, M.; Jiang, H. Aerodynamic Interference Effect of Single Surrounding Building on Average Wind Pressure of Industrial Plant Roof. *J. Build. Struct.* **2011**, *32*, 24–32.
2. Van Hooff, T.; Blocken, B. On the effect of wind direction and urban surroundings on natural ventilation of a large semi-enclosed stadium. *Comput. Fluid* **2010**, *39*, 1146–1155. [CrossRef]
3. Akon, A.F.; Kopp, G.A. Mean pressure distributions and reattachment lengths for roof-separation bubbles on low-rise buildings. *J. Wind Eng. Ind. Aerodyn.* **2016**, *155*, 115–125. [CrossRef]
4. Holmes, J.D. Wind pressures on tropical housing. *J. Wind. Eng. Ind. Aerodyn.* **1994**, *53*, 105–123. [CrossRef]
5. Quan, Y.; Gu, M.; Tamura, Y.; Huang, P. Interference effect of Surrounding Buildings on wind pressure of low building roof. *J. Tongji Univ. (Nat. Sci. Ed.)* **2009**, *37*, 1576–1580.
6. Chang, C.H.; Meronry, R.N. The effects of surroundings with different separation distances on surface pressures on low-rise buildings. *J. Wind Eng. Ind. Aerodyn.* **2003**, *91*, 1039–1050. [CrossRef]
7. Yong, C.K.; Yoshida, A.; Tamera, Y. Characteristics of surface wind pressures on a low-rise building located among a large group of surrounding buildings. *Eng. Struct.* **2012**, *35*, 18–28.
8. Zhong, H.-y.; Lin, C.; Shang, J.; Sun, Y.; Kikumoto, H.; Ooka, P.; Qiana, F.-P.; Zhao, F.-Y. Wind tunnel experiments on pumping ventilation through a three-story reduce-scaled building with two openings affected by upwind and downwind buildings. *Build. Environ.* **2022**, *219*, 109188. [CrossRef]
9. Yong, C.K.; Tamera, Y.; Yoon, S.W. Proximity effect on low-rise building surrounded by similar-sized buildings. *J. Wind Eng. Ind. Aerodyn.* **2015**, *146*, 150–162.
10. Liu, Z.; Yu, Z.; Chen, X.; Cao, R.; Zhu, F. An investigation on external airflow around low-rise building with various roof types: PIV measurements and LES simulations. *Build. Environ.* **2020**, *169*, 106583. [CrossRef]
11. Tominaga, Y.; Akabayashi, S.; Kitahara, T.; Arinami, Y. Air flow around isolated gable-roof buildings with different roof pitches: Wind tunnel experiments and CFD simulations. *Build. Environ* **2015**, *18*, 204–213. [CrossRef]
12. Quan, Y.; Gu, M.; Tamura, Y.; Huang, P.; Masahiro, M. Interference factors of surrounding buildings on Wind Load of flat roofs of Low Buildings. *J. Civ. Eng.* **2010**, *43*, 20–25.
13. Guirguisa, N.M.; El-Aziz, A.A.A.; Nassief, M.M. Study of wind effects on different buildings of pitched roofs. *Desalination* **2007**, *209*, 190–198. [CrossRef]
14. Li, Z.; Zhong, M.; Hu, L. Wind tunnel test on low-rise buildings influenced by spacing between hillside and building in typical mountain terrain. *Build Struct* **2015**, *36*, 67–74.
15. Zhong, M.; Huang, B.; Li, Z.; Zhou, Z.; Liu, Z. Study on fluctuating wind pressure distribution and probabilistic properties of low-rise buildings affected by slope gradient in mountain forms. *Symmetry* **2022**, *14*, 2513. [CrossRef]
16. Mostafa, K.; Zisis, I.; Stathopoulos, T. Codification of wind loads on hip roof overhangs of low-rise buildings. *Eng. Struct.* **2023**, *288*, 116199. [CrossRef]
17. Abdelfatah, N.; Elawady, A.; Irwin, P.; Chowdhury, A.G. Experimental investigation of wind impact on low-rise elevated residences. *Eng. Struct.* **2022**, *257*, 114096. [CrossRef]
18. Ong, R.H.; Patruno, L.; Yeo, D.; He, Y.; Kwok, K.C. Numerical simulation of wind-induced mean and peak pressures around a low-rise structure. *Eng. Struct.* **2020**, *214*, 110583. [CrossRef]
19. Qiu, Y.; San, B.; Zhao, Y. Numerical Simulation and Optimization of Wind Effects of Porous Parapets on Low-Rise Buildings with Flat Roofs. *Adv. Civ. Eng.* **2019**, *2019*, 3402613. [CrossRef]
20. Jameel, A.; Irtaza, H.; Javed, M.A. Study of wind forces on low-rise hip-roof building. *Int. J. Eng. Sci. Technol.* **2015**, *7*, 43–53. [CrossRef]
21. Honerkamp, R.; Yan, G.G.; Van De Lindt, J. Revealing Bluff-Body Aerodynamics on Low-Rise Buildings under Tornadic Winds Using Numerical Laboratory Tornado Simulator. *J. Struct. Eng.* **2022**, *148*, 04021294. [CrossRef]
22. Hnaien, N.; Hassen, W.; Kolsi, L.; Mesloub, A.; Alghaseb, M.A.; Elkhayat, K.; Abdelhafez, M.H.H. CFD Analysis of Wind Distribution around Buildings in Low-Density Urban Community. *Mathematics* **2022**, *10*, 1118. [CrossRef]
23. Sharma, D.; Pal, S.; Raj, R. Effect of spacing on wind-induced interference on the roof of low-rise buildings with cylindrical roof using CFD simulation. *Sādhanā* **2023**, *48*, 283. [CrossRef]
24. Singh, J.; Roy, A.K. CFD simulation of the wind field around pyramidal roofed single-story buildings. *SN Appl. Sci.* **2019**, *1*, 1–10. [CrossRef]
25. Singh, J.; Roy, A.K. Effects of roof slope and wind direction on wind pressure distribution on the roof of a square plan pyramidal low-rise building using CFD simulation. *Int. J. Adv. Struct. Eng.* **2019**, *11*, 231–254. [CrossRef]
26. Ministry of Housing and Urban-Rural Development of the People's Republic of China. *Load Code for the Design of Building Structures*; China Architecture & Building Press: Beijing, China, 2012.
27. Sun, Y.; Xu, N.; Wu, Y. Spectral model of fluctuating wind pressure on grandstand roofs with consideration of signature turbulence. *J. Build. Eng.* **2010**, *31*, 24–33.
28. Qiu, T.; Zhang, X.; Li, X. *Statistical Signal Processing–Non-Gaussian Signal Processing and Its Applications*; Publishing Housing of Electronics Industry: Beijing, China, 2004.
29. Gioffrè, M.; Gusella, V.; Grigoriu, M. Non-Gaussian wind pressure on prismatic buildings. I: Stochastic field. *J. Struct. Eng.* **2001**, *127*, 981–989. [CrossRef]

30. Wu, Y. Research on Wind Effect and Wind Resistance Design Theory of Large Span Roof Structures: A Postdoctoral Research Report from Tongji University. Ph.D. Thesis, Tongji University, Shanghai, China, 2006.
31. Kumar, K.S. Computer Simulation of Fluctuating Wind Pressures on Low Building Roofs. *J. Wind. Eng. Ind. Aerodyn. J. Int. Assoc. Wind. Eng.* **1997**, *69–71*, 685–695. [CrossRef]
32. Cui, L.; Peng, X.; Shi, L. Computational Domain Setting about Numerical Wind Tunnel in the Simulation of the Low-Rise Housing in the Mountain. *J. Huaqiao Univ. (Nat. Sci.)* **2010**, *31*, 463–467.